

Chapter 1 The Tracking Detector

1.1 Introduction

The tracking detector is located in the uniform magnetic field (1T) region of the detector solenoid (DS). This detector is designed to measure with good efficiency the parameters of the helical trajectory of those electrons emitted from the stopping target within the angular acceptance of the detector and having momenta near 105 MeV/c. The uncertainty in the helical parameter measurements is dominated by multiple scattering in the tracker. A second source of uncertainty in the energy measurement is associated errors in pattern recognition. This later source does not reduce the acceptance significantly, but is a serious background because it can generate high energy tails in the resolution function. In addition to these errors, obtaining the initial electron energy from the helix depends on knowing the energy loss in the stopping target and in the amount and type of material through which the electron passes (e.g. proton absorbers). Energy loss has two effects. One is to broaden the central part of the resolution function and to introduce a small mean energy loss. The second is to produce a low energy tail. This latter effect is essentially equivalent to a loss of detector acceptance.

A “good geometry” spectrometer should measure the radius of the projected circular pattern of the electron with minimal error. In the MECO detector, spatial resolution does not contribute significantly to the energy resolution. A minimum of three position measurements is required, but more points are needed to over constrain the fit and reduce backgrounds. This is particularly important because additional signals, noise clusters, and inefficiencies in the detectors can be combined with true signals to yield a trajectory that reconstructs with energy in the μ - e conversion region (105 MeV). These general design considerations lead to two possible detector geometries;

- 1) a longitudinal tracker (T-Tracker); and
- 2) a transverse tracker (L-tracker).

The T-tracking detector consists of a set of straw planes placed so that the axial direction of the straw is transverse to the axis of the solenoid. Each plane has a set of 4 trapezoidal straw tube arrays. Each array has a width of 30cm and is composed of 60 straw tubes of 5 mm diameter varying in length between 70 and 130 cm. Depending on further R&D reliability studies, the straw walls will be either 15 or 25 μ m thick. The arrays are positioned on each plane so that the central square region of the detector, having dimensions (2 x 38 cm) x (2 x 38 cm), does not contain active detector elements, Figure ~\ref{fig_T_Tracker}. Each plane is azimuthally rotated by 60 degrees around the central axis. There are 54 planes extending over an approximate 3.2m axial distance in order to accept 2 full helical turns of the electron trajectories of interest.

In the T-tracker, a hit location in the coordinate transverse to the straws is determined by the straw position and the drift time, and the hit position in the axial direction is determined by the plane position. There is presently no second coordinate readout in this detector, although charge division on the straw anodes is under consideration. The azimuthal position is obtained from the stereo angle between the rotated tracking units. Both timing and pulse height information is recorded for each hit wire, in order to discriminate low-energy proton “hits” from minimum ionizing electrons. The number of straws and readout channels for the T-Tracker is given in Table ~\ref{tab_T-channels}.

The L-tracker consists of an octagonal array of planes of tracking detectors placed symmetrically around the axis of a magnetic solenoid, Figure ~\ref{ltrk1}. In addition there are 8 tracking planes (referred to as vanes), projecting radially outward from each vertex of the octagon. Each octagonal plane and vane is approximately 30 cm wide, 260 cm long, and composed of 3 layers of 5mm diameter, close-packed straw tubes. Extensive studies have been done for 2.4 m and 2.9 m long detectors. For a 2.4 m detector, 39% of conversion electrons emitted with $p_t > 91$ MeV/c have at least 6 hits in the tracking detector; a 2.9 m detector guarantees that two full helix turns are measured for the same class of events. A straw tube plane/vane is constructed of 2 straw layers with resistive cathode walls, sandwiching a conducting straw layer. This design is shown in Figure ~\ref{ltrk_2}. The resistive cathodes allow the signal charge collected on the anode wires to image on a plane of conducting strips aligned perpendicular to the straw axis. These strips are 4mm wide, separated by a 1mm. A hit position in the radial and azimuthal direction is then determined by the straw position and the drift time on the anode (wire). The hit position in the axial direction is determined by the centroid of the imaged charge on the cathode strips. The straw walls are assumed to be 30 μ m thick. There are a total 1920 resistive cathode straws, 960 conductive cathode straws, and 16,640 cathode strips. The number of electronic channels which must be readout in this detector is given in Table ~\ref{tab_L-channels}. To minimize multiple hits on the same detector element due to particles spiraling along a magnetic field line, the planes and vanes of the L-tracker are rotated about a perpendicular axis to a field line by a small angle (typically 15 mrad).

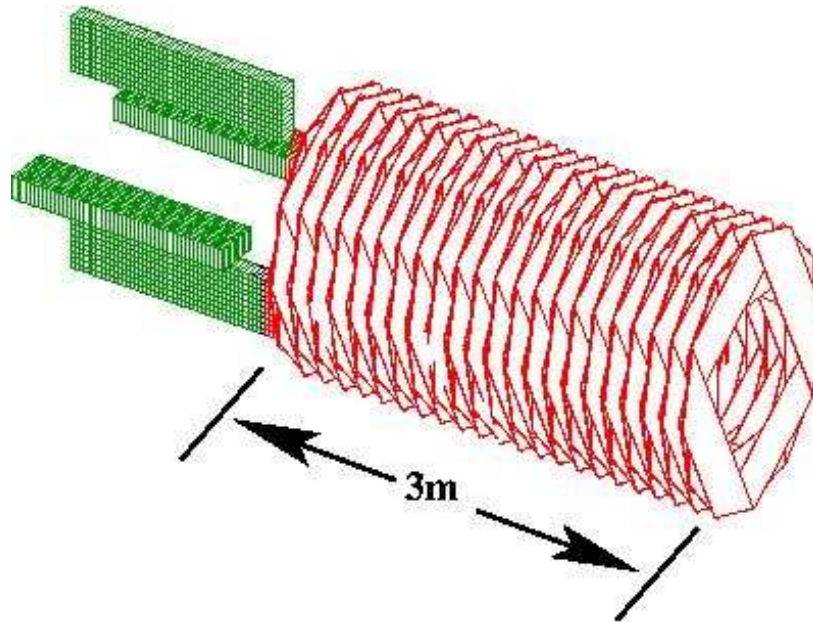


Figure 1.1: A perspective view of the MECO T-tracker showing the straw frames as they are azimuthally rotated and the position of the calorimeter.

Straw Tubes	Number of Straws	Readout (TDC)	Readout(ADC)
Per Plane (60 x 4)	240	240	240
Per Module (3 planes)	720	720	720
Per Detector (18 Modules)	12,960	12,960	12,960

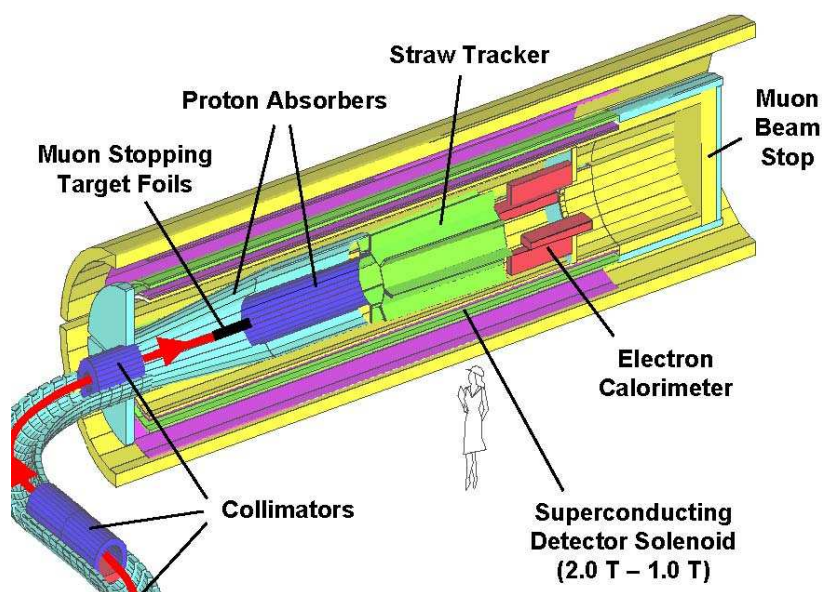


Figure 1.2: A perspective view of the L-tracker showing the detectpr solenoid, stopping target, calorimeter, and beam dump.

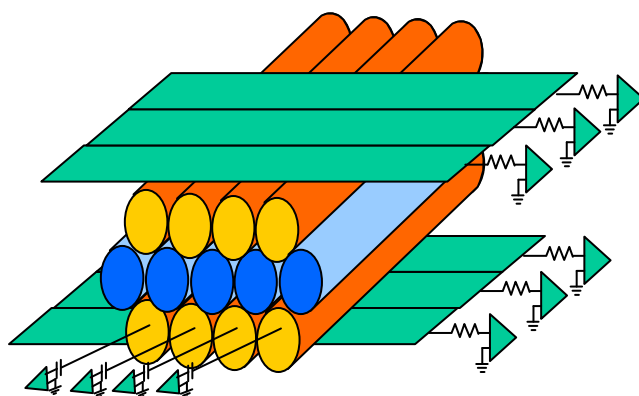


Figure ~\ref{strips} A section of an L-Tracker plane showing the close packed straws, the resistive cathode straws, the conducting cathode straw, and the induction strips.

Element	Component	Number/Element	TDC Readout (8 elements)	ADC Readout (8 Elements)
Cylindrical Plane	Straw	192	1536	1,536
	Cathode Strips	1,040	8,320	8,320
Vane Plane	Straw	152	1,216	1,216
	Cathode Strips	1,040	8,320	8,320
Total Detector			19,392	19,392

1.2 Tracking Detector Performance

1.2.1 General Resolution Requirements

The limiting electron background in the MECO experiment is muon decay in orbit (DIO). The endpoint of the DIO spectrum is the energy of the electrons which would be emitted in coherent muon conversion. Both the absolute normalization and the energy spectrum are calculated [43, 44] and these calculations agree to a precision of about 25%. The small discrepancy in these calculations can be traced to different approximations when including nuclear recoil effects and relativistic corrections to the muon wave function. The DIO spectrum falls as the fifth power of the difference between the endpoint energy and that of the DIO electron, so the level of background under a mono-energetic conversion electron peak is very sensitive to resolution. Thus to reduce background, the central part of the resolution function must be minimized and all high energy tails suppressed.

To find the constraints on the width of the resolution function and its high energy tails, we define the detector response function as $f(x)$, where x is the difference of the detector-reconstructed energy and the conversion energy, $x = E_{det} - E_0$. Generally, $\int_{-\infty}^{\infty} f(x) dx < 1$, due to finite acceptance. If one defines the signal region as $x > \Delta$, then one can define an acceptance function $A(\Delta)$ as;

$$A(\Delta) = \int_{\Delta}^{\infty} f(x) dx .$$

Assuming the normalized background takes the form [44] ;

$$dn/dE = C(-x)^5 \quad (x < 0) .$$

with $x < 0$, one can define a noise function $N(\Delta)$ as;

$$\begin{aligned} N(\Delta) &= \int_0^{\infty} C x^5 dx \int_{x+\Delta}^{\infty} f(y) dy \\ &= \int_{\Delta}^{\infty} C/6 [y-\Delta]^6 f(y) dy . \end{aligned}$$

One can further define a noise/signal ratio, R , as;

$$R(\Delta) \equiv \frac{N(\Delta)}{B_{\mu e} A(\Delta)} .$$

Here $B_{\mu e}$ is the μe conversion branching ratio, taken to be 10^{-16} in the following studies. Estimates of C are inferred from the references [43, 44], and the value of $C \approx 0.6 \times 10^{-16} \text{ MeV}^{-6}$ is used here. Signal to background improves Background with the sixthpower of the resolution, so even small improvements in resolution are of great importance.

Figure 1.1 shows the acceptance as a function of σ using a Gaussian detector resolution function, with a Background/Signal ratio of 0.05. Compared with the acceptance for a perfect detector with $\sigma = 0$, the acceptance is 90% at $\sigma = 300 \text{ keV}$, and 70% at $\sigma = 400 \text{ keV}$. The acceptance drops quickly for $\sigma > 400 \text{ keV}$. Thus, we require $\sigma < 400 \text{ keV}$, or FWHM $< 1 \text{ MeV}$. Constraints on the magnitude of a high energy tail can be qualitatively inferred from Equation 9.2. To illustrate, if we require the extra background contribution from the high energy tail to be less than 2% of the acceptance, then the magnitude of any high energy tail above ΔE should be less than $0.2 \times \Delta E^6 [\text{MeV}^{-6}]$; e.g., a high energy tail above 5 MeV should be less than 10^{-5} .

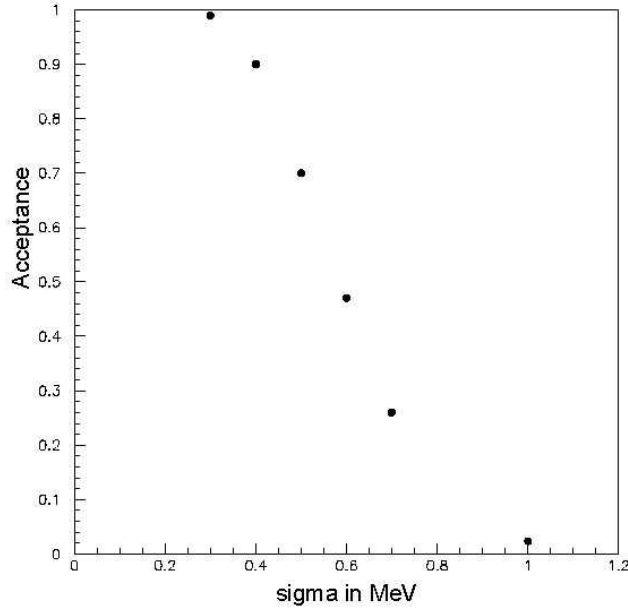


Figure 1.1: Acceptance as a function of σ , using a Gaussian detector resolution function; assuming $R_{\mu e} = 10^{-16}$ and Background/Signal=0.05. The acceptance is normalized to 1 for a perfect detector, $\sigma = 0$.

1.2.2 Detector Rates

High rates in the detector may limit the experimental sensitivity in several ways. First, detector occupancy could be so high that the efficiency of obtaining valid position information is reduced. This problem may be mitigated by increasing detector granularity and time resolution. Second, noise (accidental) hits may be combined with those of a lower energy electron (DIO) trajectory to create an event consistent with the energy of a conversion electron (105 MeV). This is a problem common to many high rate experiments that look for rare events, and it may be suppressed by increasing the time resolution, increasing the redundancy in position measurements, and by analyzing only hits from the

particles of interest (particle ID). Third, there may be contributions to the trigger rate due to pile-up of lower energy signals in the trigger detector. This possibility may be addressed by increased segmentation, optimizing the geometric design, and by appropriate pulse shaping and timing.

A high flux of charged particles passes through the muon beam channel and the detector solenoid during, and for a 200 ns window after, the beam spill. Between proton pulses, we require that a negligible number of protons hit the production target, so the secondary particle flux passing through the beam channel is low. Therefore the detector is active (read out) only during the last 650ns between each proton beam spill. We also note that the magnetic field is designed to avoid traps which could result in the arrival of particles in the DS after the active window opens, and to prevent particles from making multiple passes through the detector.

During the active time window, detector rates arise from four main sources.

- Muon DIO

These electrons form the primary background to the measurement, and the detector and graded magnetic field are designed so that the majority of these electrons ($< \sim 60$ MeV/c), have helical radii less than 38 cm. These then pass unobserved through the central “hole” in the detector.

- Photons and nuclear particle emission

Roughly 60% of the stopped muons are captured on nuclei. These captures produce photons, neutrons, and protons from nuclear de-excitation. Approximately 2γ 's, 2 neutrons, and 0.1 protons are emitted on average for each capture. The proton flux from the target is reduced by placing polyethylene absorbers in appropriate positions before the tracking detector. Neutrons are absorbed by boron or Li impregnated polyethylene blocks placed on the cryostat walls.

- Target bremsstrahlung

Beam electrons emit bremsstrahlung radiation as they traverse the stopping target. These photons may Compton scatter and pair produce in the detectors. The pulsed beam and the muon beam line are designed to reduce the flux of low-energy electrons that reach the stopping target during the active time window.

- Muon albedo from the beam stop

Muon albedo from muon interactions in the beam stop can reach the detector, but the design of the beam stop significantly reduces these rates. In addition, although the number of muons reaching the dump is approximately half the total flux in the beam, the probability of a “hit” in the detector from a muon that decayed in the dump is significantly less than that of a muon decaying in the stopping target.

The detector design is driven by the need to be insensitive to the majority of the approximately 10^{11} muon decays per second. This is an advantage of $\mu^- N \rightarrow e^- N$ experiments with respect to $\mu \rightarrow e\gamma$, since the signal electrons appear at the endpoint of the spectrum (105 MeV as is shown in) rather than at its center. To simulate detector rates from DIO, electrons were spatially generated in accordance with the stopping distribution in the target. The DIO spectrum is shown in figure 1.2 and tabulated in Table 1.1.

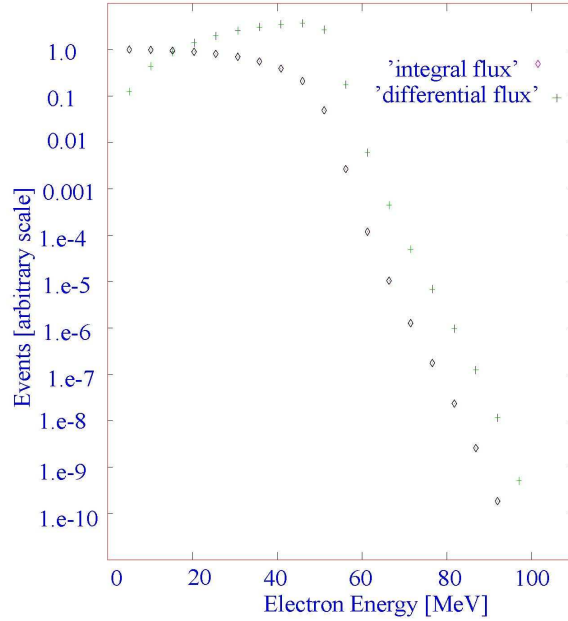


Figure 1.2: Plot of the differential and integral electron energy distributions for μ decay in orbit. Circles are the integral of the distribution for energies above the abscissa value, and crosses are the differential distribution. The background-type symbols are explained in Subsection 8.6.3.

Table 1.1: The integrated flux of DIO electrons above various energies.

Lower energy limit (MeV)	Total DIO events
100	1×10^5
95	5×10^6
90	1×10^8
85	1×10^9
80	9×10^9
75	6×10^{10}

In addition to DIO, the background includes protons and photons from nuclear de-excitation following muon capture, electrons traversing the detector, and bremsstrahlung photons that pair produce or Compton scatter in the tracking detector (often after first scattering somewhere else in the detector solenoid). For simulation, these particles are chosen isotropically with the appropriate energy distribution, and tracked through the magnetic field. The energy spectra of particles emitted from nuclei following muon capture and the electron spectrum of muon DIO are taken from the literature.

Total detector rates are calculated using GEANT simulations including all components that are in the interior of the detector solenoid. The most important physical processes in the materials of the detector solenoid, and muon beam dump were included. Some of the rates depend on the amount of material in

the tracking detector, and this has been modeled in some detail, including the structure supporting the straws, cabling, etc. Contributions to the tracker rates in both the T- and L-trackers are shown in Table 1.3.

In more detail, every μ^- capture results in the production of excited nuclear states, radioactive nuclei, and/or neutron emission with the possibility of subsequent neutron induced nuclear gamma rays. This results in photons originating from various places in the detector solenoid, some fraction of which are not associated with the beam gate. Almost all of these photons are less than a few MeV (the binding energies of the most probable excited nuclei after μ^- capture are less than 4 MeV). We analyze the effects of a photon energy spectrum from 0 to 10 MeV at a rate of 1.8 photons per μ^- capture.

Table 1.3: Peak detector rates R_{wire} at the beginning of the measurement window 700- 1350 ns. The average number of hits from one background particle in the whole detector is $\langle N_{event} \rangle$.

background type	background rate, Hz	probability to hit detector	$\langle N_{event} \rangle$	R_{wire} , kHz
e_t	2.7×10^{11}	0.00032	1.54	65
n_t	2.43×10^{11}	0.000142	2.887	49
γ_t	2.43×10^{11}	0.000248	4.524	134
p_t	0.181×10^{11}	0.00362	6.263	202
$eDIO_t < 55$	0.795×10^{11}	9.8×10^{-5}	1.44	5.5
$eDIO_t > 55$	2.07×10^8	0.00127	22.7	2.1
n_{bd}	0.475×10^{11}	7.1×10^{-5}	5.0	5.9
γ_{bd}	0.475×10^{11}	8.3×10^{-5}	4.5	6.1
$eDIO_{bd} < 55$	2.1×10^{11}	8.9×10^{-5}	1	6.6
$eDIO_{bd} > 55$	5.46×10^8	1.82×10^{-4}	1.5	0.05
$eDIF$	2.74×10^6	1	35.84	34.5
total				464

Protons are also emitted during the μ^- capture process, and are the potentially most serious background contribution [cite{tracker_comp}]. The proton spectrum, which has energies predominately below 15 MeV, was taken from experiment [95] where muons were stopped in emulsion. The shape of this spectrum is almost Gaussian, centered at ~ 7.5 MeV proton energy, having a ~ 5.5 MeV width and a high energy tail extending above 50 MeV. The normalization is somewhat uncertain and depends strongly on nuclear size. The best available data on the normalization is from Budyashov et al. [96], although other experiments [97, 98, 99, 100] report measurements on various nuclei. We choose a conservative approach by using the largest reported flux, 0.15 protons per μ^- capture. The proton spectrum is shown in Figure 1.6. Although these protons have relatively high momentum, they have low kinetic energy and are easily absorbed.

Using the above proton production fraction, the total instantaneous flux of protons exiting the stopping target is $\approx 1.6 \times 10^{10}$, and without shielding the average rate in the individual tracking detector elements would be well above 1 MHz. However, protons can be significantly attenuated by a set of absorbers placed between the target and the front of the detector. These absorbers are designed as a conic, cylindrical shell of polyethylene and ployethelyne blocks. Particle rates in the trackers are given in Table~\ref{t.trk.rates}.

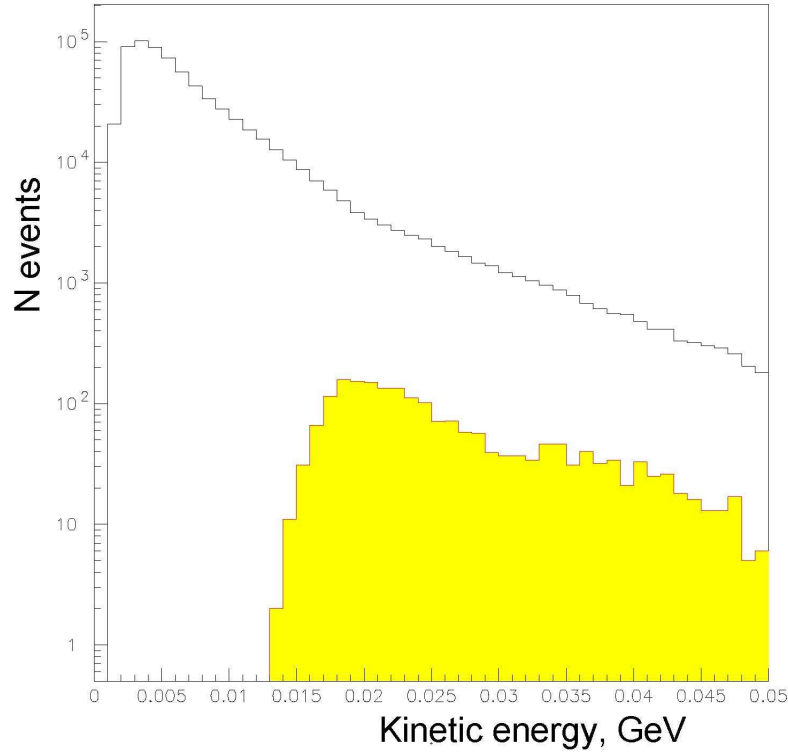


Figure 1.6: The distribution of the kinetic energy of protons originating from μ^- capture on Al, taken from a fit to the data of reference [95]. The shaded histogram gives the distribution of protons that cause hits in the tracking detector. One may note the attenuation of low energy protons in the proton absorbers described in Section 8.3.

The effect of proton absorption in the stopping target and the absorbers is shown in Figure 1.6. The lowest momentum protons are fully absorbed, but the remaining protons typically have a mean ionization rate $\sim 25 \times$ minimum-ionizing.

Late arriving beam electrons also cause detector hits. These have been calculated in a GEANT simulation using the time and energy distribution of beam electrons as discussed in Chapter 8. The hits come from bremsstrahlung in the stopping target, with the γ 's subsequently Compton scattering or producing pairs in the tracker. This contribution is given in the first line of **Error! Reference source not found.** We note that late arrivals are reduced by the improved design of the muon beam.

Finally, neutrons are produced during the μ^- capture process. A neutron spectrum, typical for our target, can be created from experimental data [101, 102]. Neutrons below 10 MeV are represented by a thermal distribution having an exponential tail above 10 MeV. Detector rates are calculated assuming two neutrons are emitted per μ^- capture.

The rate of neutron hits is sensitive to the detailed geometry of the detector solenoid, but the present simulation suffers from the fact that neutrons are tracked only down to 10 keV, at which point they deposit their remaining energy locally. We have recently begun to use the GCALOR code, and we plan to explore other codes as well. The neutron flux is attenuated by insertion of appropriate neutron absorbers, for example in the region upstream around the stopping target and outside the conical proton absorber.

The total rate per detector element is ~ 500 kHz for 40Tp in an AGS spill, and this rate is lower than that in straw chambers of similar construction. During a 30 ns gate with a typical drift velocity of $100 \mu\text{m/ns}$, the average occupancy will be under 2%. In any event, the AGS intends to deliver only half of this intensity to the experiment. In addition, many of the signals induced by these particles may be distinguished from those induced by conversion electrons, and thus it is possible to selectively discriminate against various background events, as outlined in the list below.

1. Hits by protons have large pulse height compared to conversion electrons.
2. Hits by electrons from Compton scattering and pair production typically have high pulse height since these make multiple turns through a single straw in the L-Tracker.
3. Hits can be distinguished by their time structure which will not be consistent with that of a spiraling 105 MeV electron.
4. Hits due to neutrons high energy deposition and will typically not activate all three layers of a straw tube plane in the L-tracker.

1.2.3 Response of the Straw Detector to Ionizing Events

The simulation of drifting ionization deposited by the movement of a charged projectile through various media has been reported in many previous studies\cite{drift_papers}. For example, the code, GARFIELD, is available from the CERN library\cite{cern}. We have adapted our own code, previously used to determine the drift time contours in a wire chamber embedded in a magnetic field, for this purpose. In general, this simulation calculates, for either of the proposed MECO geometries, the charge collected on the anode wire as a function of drift time. The ionization, represented by a Vavilov distribution\cite{vavilov}, is a Poisson process deposited along the trajectory. The projectile and drifting ionization move under the influence of the magnetic field.

The simulation drifts electrons under the influence of the local \mathbf{E} and \mathbf{B} fields, mapping the drift motion of each ionization cluster, and collecting the charge as a function of time on the straw tube anodes. Recombination of the drift charge is ignored but diffusion is included. The drift time vs position for each track is determined by recording the first arrival time of a drifting cluster as a function of the closest distance of approach of the incident track to the anode wire. The first electron arrival cannot be directly measured, as the charge arrives in clusters and the discrimination threshold must be set above a cluster size of one electron. In any event, the readout electronics integrates the signal over ≈ 15 ns, but it is possible to use the pulse shape to extrapolate the time from the threshold measurement backwards to the first arrival time.

A charged particle ionizes the medium through which it travels, depositing on average, an energy loss given by the Bethe-Bloch equation\cite{eloss}. However, the number of atomic collisions along a path is given by a Poisson distribution\cite{drift_papers}. The energy loss of the traversing particle is obtained from the energy expended in the ionization, and the kinetic energy imparted to the ionized electrons. All of this energy is deposited in the medium if photons from the de-excitation of the ionized atoms are absorbed and the ionized electrons are stopped in the medium. The average energy loss depends on the medium, the projectile velocity, and the charge, having a minimum value\cite{dc_book} (minimum ionizing particle or MIP) when the relativistic γ factor of the projectile is ≈ 3.5 -4.0. The number of clusters and primary electrons per cm-atmosphere for a MIP, produced in various gases are

listed in Table ~\ref{tab:ion}. A global fit of the ionizing potential as a function of the atomic charge of the material\cite{barcus}, Z , is;

$$I(\text{ev}) = 9.76 Z + 58.8 Z^{-0.19}.$$

The effective ionization potential for a molecule can then be estimated from the equation;

$$\langle \ln[I(\text{ev})] \rangle = [\sum F(\text{wt})_k Z_k \ln(I_k)] / [\sum F(\text{wt})_k Z_k]$$

The number of clusters and total pairs/cm produced by a MIP in various gases

Gas	Clusters/cm	Total Pairs/cm
H ₂	5.2	9.2
He	5.9	7.8
Ne	12.0	39.0
Ar	29.4	94.0
Kr	22.0	192.0
Xe	44.0	307.0
CO ₂	34.0	91.0
C ₂ H ₆	21.0	103.0
CH ₄	12.0	53.0
CF ₄	41.0	180.0
C ₄ H ₁₀	46.0	195.0

In the above expression $F(\text{wt})_k$ is the fractional atomic weight for the k^{th} atom of the molecule, Z_k is its charge, and I_k is its ionization potential. The average energy loss may then be determined from the relativistic Bethe-Bloch equation using the density of the gas, the ionization potential and the β of the incident particle.

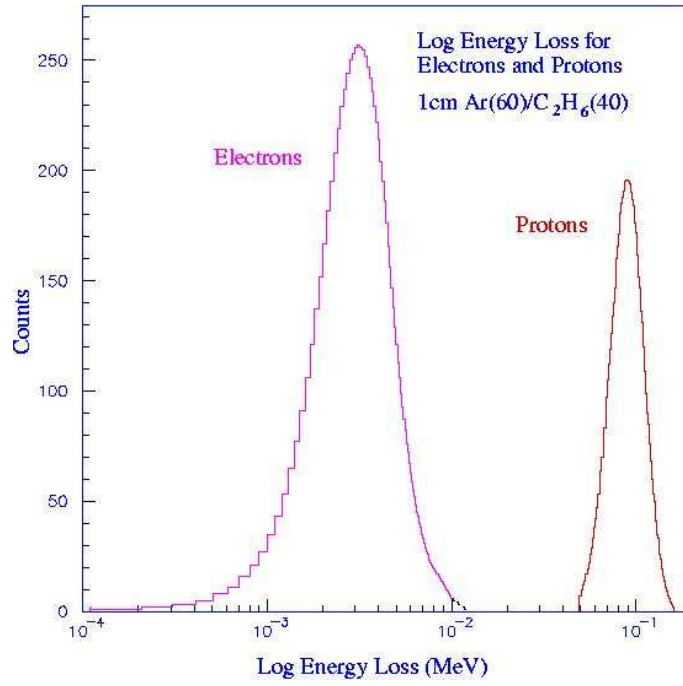
An example of an energy loss calculation, Fig. \ref{fig:eloss}, shows the simulated energy loss for electrons and protons with momenta of 100 MeV/c in 5mm of a chamber gas consisting of 60% Ar and 40% C₂H₆. Note that the energy scale is logarithmic.

To study the drift equations in the presence of a magnetic field, we assume that the direction and velocities of the drifting electrons can be obtained from the application of the Lorentz force with the addition of a dissipative term, representing resistive flow (collisions). The solution to the equilibrium equations for \mathbf{B} in the \mathbf{z} direction is;

$$V_x = \epsilon_x \omega \sin(\omega t) ;$$

$$V_y = \epsilon_x \omega (\cos(\omega t) - 1);$$

$$V_z = \epsilon_z t ;$$



The figure shows the calculated energy loss for electrons and protons with 100 MeV/c momentum in a gas mixture of 70% Ar and 40 % C₂H₆. Note the logarithmic scale of the energy loss.

where $\epsilon = (e/m)\mathbf{E}$, and $\omega = (e/m)\mathbf{B}$. As the electron moves through the gas, the probability of a collision is;

$$f(t) = (1/\tau) E^{-t/\tau};$$

where τ is the mean time between collisions. We then obtain for the average drift velocities;

$$u_x = \langle v_x \rangle = (\epsilon_x \tau) / [1 + (\omega \tau)^2]$$

$$u_x = \langle v_x \rangle = (-\epsilon_x \tau^2) / [1 + (\omega \tau)^2]$$

$$u_x = \langle v_x \rangle = (\epsilon_z \tau)$$

In these expressions we have neglected diffusion to simplify the presentation, but this is included in the numerical simulation. We do not include the statistical distribution of electron velocities.

The geometry for the L-tracker assumes \mathbf{B} lies in the z direction, and the \mathbf{E} field is in the (x,y) plane with θ the angle of \mathbf{E} with respect to the x axis. Transforming the above drift equations into polar coordinates in the (x,y) plane one obtains;

$$u_r = (\epsilon_x \tau) / [1 + (\omega \tau)^2]$$

$$u_\theta = \omega \tau / [1 + (\omega \tau)^2]$$

Obviously the Lorentz angle, α , for the L-tracker is then;

$$\tan(\alpha) = \omega\tau$$

There is no drift velocity along the **B** field (z direction).

The geometry for the T-tracker assumes **B** lies in the z direction, and the **E** field is in the (x,z) plane with θ the angle of **E** with respect to the x axis and y the direction along the anode wire of the straw detector. Transforming the above drift equations into polar coordinates in the (x,z) plane one obtains;

$$u_r = (\epsilon\tau)[1 + \omega\tau (\sin(\theta))^2] / [1 + (\omega\tau)^2]$$

$$u_\theta = \{(\omega\tau)^2/[1 + (\omega\tau)^2]\} \epsilon \cos(\theta) \cos(\theta)$$

$$u_y = -[\{(\omega\tau)/[1 + (\omega\tau)^2]\} \epsilon \cos(\theta)]$$

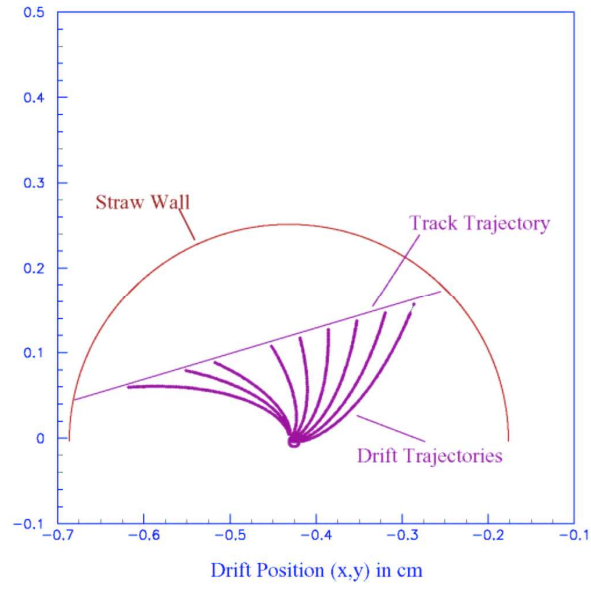
The Lorentz angle is then a complicated expression as it no longer lies in the plane containing **E**.

Drift Velocities have been measured for a number of gases and gas mixtures\cite{drift_papers}. In some cases these have been obtained as a function of an applied magnetic field. Appropriate parameters are not readily available for the gases and fields used in MECO, although one can use measured drift parameters as a function of the electric field strength in the absence of a magnetic field to extract the mean time between collisions, τ , as a function of the field, and then use the above equations to obtain the velocities in the various coordinate directions as a function of both the electric and magnetic fields. Generally this seems to produce a somewhat smaller Lorentz angle than measured, in some cases by as much as 10-20\% at higher fields. The drift velocity can be corrected for pressure differences by the square root of the pressure.

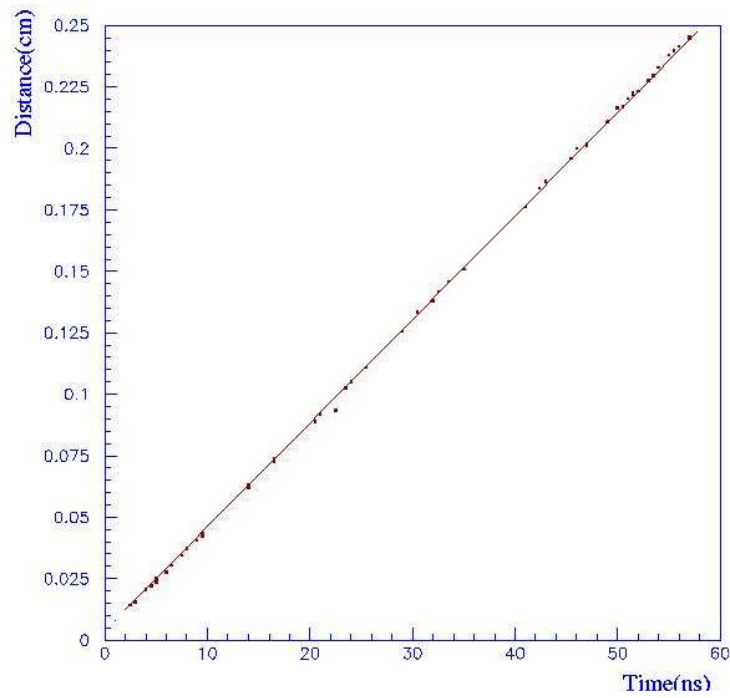
A typical drift trajectory for the L-Tracker is shown in Fig. ~\ref{fig:drift-L}. The incident electron track is obvious as well as the positions of the ionization clusters. The ionized electrons drift under the an electric field generated by a potential of ≈ 1500 V in a magnetic field of 1.2 T. Their trajectories have the expected spiral paths. The first arrival cluster time vs the distance of closest approach for this geometry is shown in Fig. ~\ref{fig:dca-L}. It is interesting that this curve is linear to good approximation, even though the first arrival cluster does not always correspond to the cluster which is nearest to the point of closest approach along the incident trajectory.

A typical drift trajectory for the T-Tracker is shown in Fig. ~\ref{fig:drift-T}. Here we provide views in the (x,z) and (x,y) planes as the drift is 3-dimensional. One can see the spread of the drift trajectories in the y direction from the original positions of ionization due to the $\vec{v} \times \vec{B}$ term of the Lorentz force. Again the first arrival time as a function of closest approach is linear as shown in Fig.

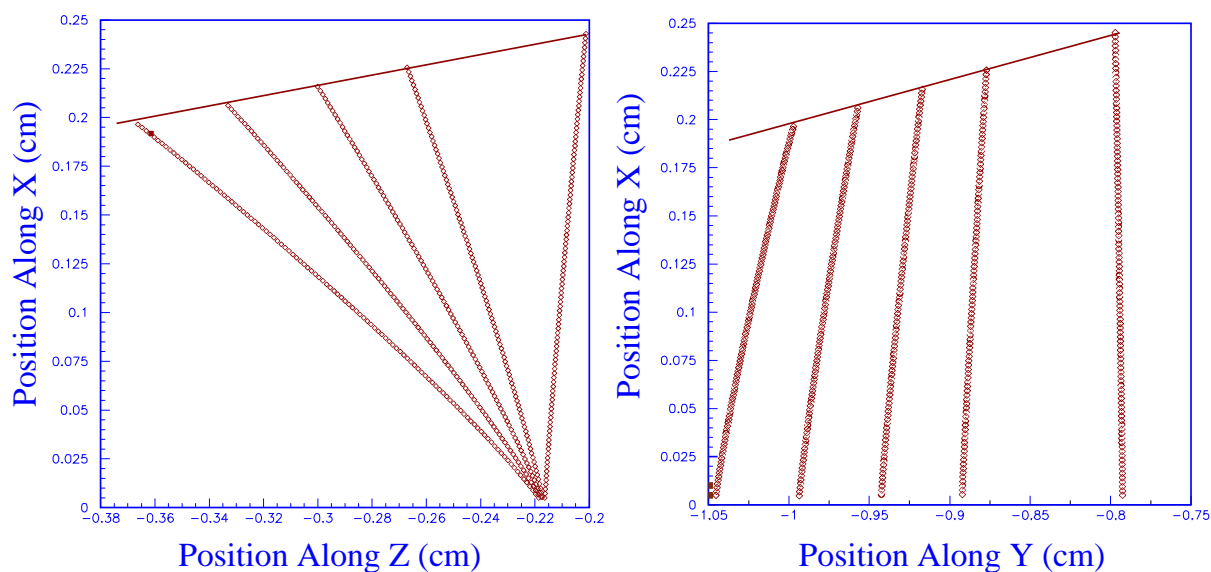
The charge collected on the anode (electrons) as a function of time is obtained from the simulation program. It is assumed that there is a linear relationship between the number of electrons collected at each time increment and the number of positive ions produced by avalanche at the anode wire. These ions are then drifted away from the anode by the ionic drift velocity creating the signal on the anode. The equations which govern this current are given in Appendix A. From these equations, the current for a cluster is calculated and is shown for one ion in Fig. ~\ref{fig:anode_c}.



The figure shows drift trajectories for a track through a straw in the L-tracker. The gas mixture is 60% Ar and 40% C_2H_6 , and the E and B fields are 1500 V and 1.2 T respectively

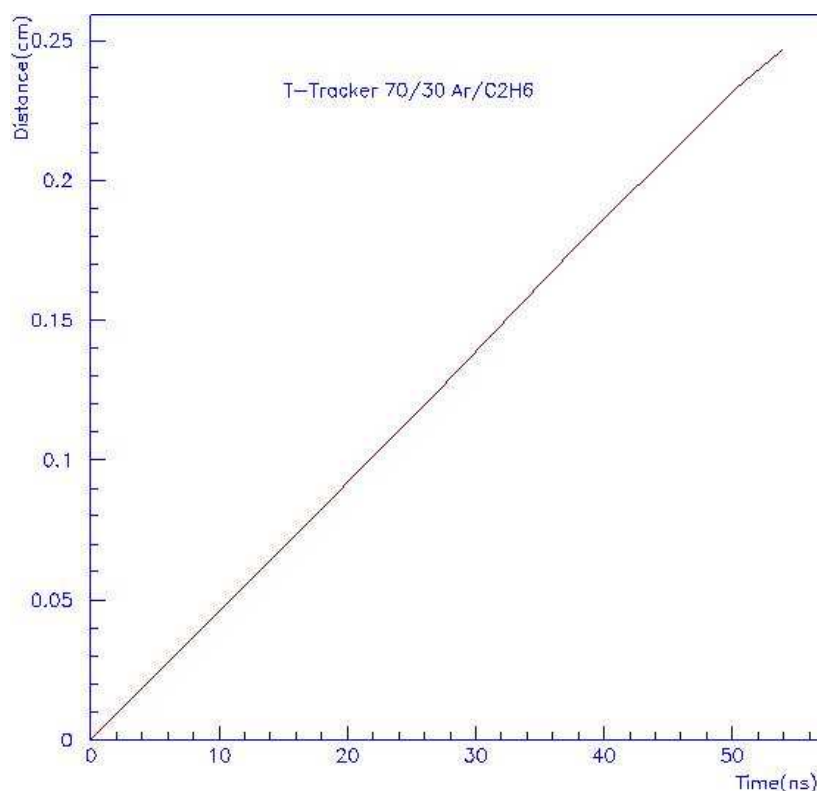


The figure shows the calculated first arrival time vs the distance of closest approach for the L-Tracker



The figure shows the calculated drift trajectories for a track through a straw in the T-tracker in both the (x,z) and (x,y) planes. The gas mixture is 60% Ar and 40% C₂H₆ and the **E** and **B** fields are 1500 V and 1.2 T respectively}

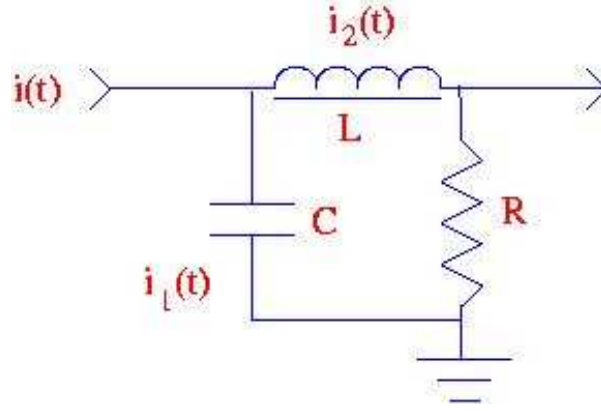
The electron current incident on the anode wire as calculated from the simulation code is then used to create positive ions as a function of time near the wire, which are then drifted away, producing the anode current. The resulting current is passed through a simple electronic filter simulating a preamplifier circuit, which imposes a bandwidth of ≈ 75 Mhz and an RC time constant of ≈ 15 ns. This filter is illustrated in Fig. ~\ref{fig:filter}. The output current, $I(t)$, is found to have the form;



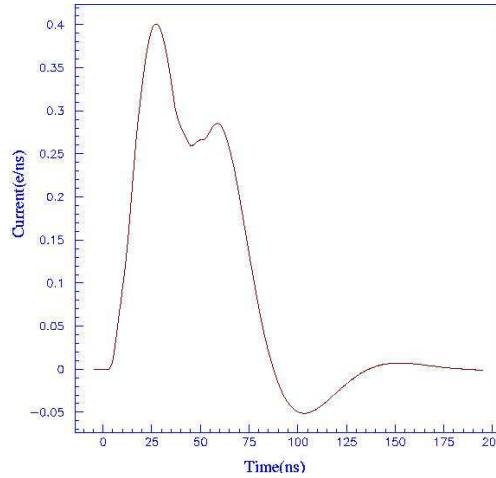
The figure shows the calculated first arrival time vs the distance of closest approach for the T-Tracker

$$I_1(t) = [1/\omega LC] \int_0^t dt' i(t') e^{-\alpha(t-t')} \sin(\omega(t-t'))$$

In this equation; $\alpha = (R/2L)$ and $\omega^2 = (1/LC)[1-(RC)^2/4LC]$. To represent the preamp, we have chosen the values; $R = 200 \Omega$, $C = 7 \times 10^{-11}$, and $L = 2.5 \times 10^{-6}$. The resulting anode current is shown in Fig ~\ref{fig:current}. The pulse shape varies by the statistical collection of the drifting electrons, but the shape is reasonably consistent with anode signals observed on an oscilloscope. The bipolar nature of the current is a consequence of the filter circuit and can be adjusted by selection of the various constants.



The figure shows the filter circuit that integrates the anode signal and imposes a bandwidth of < 75 Mhz



The figure shows the anode current for a particular electron track as calculated by the simulation

1.2.4 Response To Signal Events in the Presence of Background

In this section, we discuss the detector response to signal events embeded in background. These studies use GEANT simulations of the target and detectors [103, 45], and incorporate full Moliere scattering,

Landau fluctuations in the energy loss, and Gaussian measurement errors. About 60% of all conversion electrons hit the detector. The errors in position measurements are taken to be $\sigma_x = 0.2$ mm, $\sigma_y = 0.2$ mm and $\sigma_z = 1.5$ mm. The simulation uses isotropically emitted electrons from the target disks, spatially distributed according to the relative muon stopping probabilities.

However, the study does not include a complete model of the tracking detector. In particular, it does not include drift times and inefficiencies in the straw cells. To account for measurement error, positions of the electron trajectory-straw tube plane crossings are recorded and randomized according to the expected spatial resolutions of the detector.

Background hits from all sources are included by sampling from a file containing a large number of previously produced events. This background is then superimposed on the real events as they are generated. Since we do not simulate individual straw signals, many of the tools that could be used to reject noise have either not been incorporated into the analysis or are incorporated only in approximation. Detailed background rejection techniques are discussed in the following section on backgrounds from pattern recognition errors.

1.2.3.1 The T-Tracker

The transverse tracker description, pattern recognition and track momentum reconstruction algorithm and background study are presented in \cite{alt,alt1,alt2}. The analysis algorithm is based on a combinatorial collapse filter (CCF), which has good convergence, and provides a reasonable efficiency for momentum reconstruction. To allow for the possibility that the calculated background rates are under underestimated, we have have studied the detector response to a nominal (600 MHz) and twice nominal (12.MHz) singles rate per straw. It is pointed out that these rates are estimated assuming a 40 Tp proton spill, and this is now known to be twice the anticipated rate to be provided by the AGS. Thus the result of the studies reported here correspond to rates a factor of 2 and 4 above the expected background.

In this study, the GEANT simulation uses the following.

- The T-tracker has the 54 plane geometry described previously.
- The GEANT simulation includes the straw structure. Straws have wall thickness 15 μ m and are constructed of Kapton. Isobutane (C₄H₁₀) gas is assumed to fill the tubes. A tungsten wire with a diameter of 20 μ m is used as the straw anode. Multiple scattering and energy loss are taken into account. The initial momentum distribution of electrons entering the tracker is shown in Figure ~\ref{fig:Pin}. This distribution can be fitted by a Gaussian with a standard deviation $\sigma = 0.21\mu$ m, having an average momentum $p_m = 104.35$ MeV/c.
- The measurement uncertainties are taken into account in the Monte Carlo by assuming that the radii of the hits corresponding to a drift time are distributed normally with $\sigma = 200$ μ m.

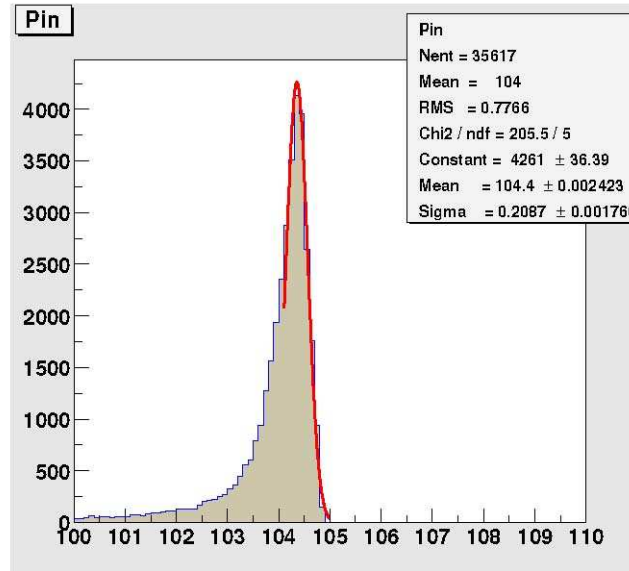
The primary sources of charged particles in the tracker detector during the detector-active window are protons, neutrons and photons from muon capture on the target nuclei and electrons from muon decay in orbit (see ~\cite{alt1} Appendix B). The average tracker rates are similar to those given in Table ~{1.3}

To study the tracker performance in the presence of the background, 100,000 muon conversion events from the target having initial electron momentum of 105 MeV/c were generated and saved to a data file.

The expected number of DIO events during the experiment time (10^7 sec) in this region is 5.2×10^4 events above 100 MeV/c. The electron spectrum at the tracker entrance is shown in figure ~{e.spect}.

To study the background, the number of simulated DIO events in this energy region was chosen to be ten times their actual number. Five different random backgrounds (protons, neutrons, photons and DIO) were generated and saved to data files. The numbers in this table are the result of GEANT simulations at twice the anticipated beam intensity. No suppression was added for the rejection of heavy ionization particles (eg protons). Nominal background was taken from the data files and added to the conversion and DIO events above 100 MeV/c. For example, the number of events for the proton background was simulated according to a Poisson distribution with average 3.1. Then the appropriate number of accidental proton events are chosen randomly from the appropriate data file and added to the muon conversion or DIO event. In the same way the above procedure is repeated for all background types. The high rate background simulation was generated by doubling the number of background events. In Figure ~{fig:nb} the distributions in the number of background hits are shown for the two background rates. In the first case the average number of background hits is 225 which corresponds to an average straw rate about 600 kHz. In the high rate case the average number of background hits is 450 which corresponds to an average straw rate about 1.2 MHz.

The analysis of an event consists of several reduction stages to extract the “true” helical hits. In the first pattern recognition stage, straw centroids are used without drift time data. In the second stage, the straw drift time data are included. At this second stage a deterministic annealing filter (DAF) ~{cite{daf}} was applied to make a final background suppression and provide a starting point for track momentum reconstruction based on a combinatorial collapse filter, CCF.



Momentum distribution of electrons entering the tracker.

The first step in the analysis is to use the centroids of the hit straws to reduce background and obtain an initial set of helical parameters. It is worthwhile to note that only the straw hits are sufficient to reconstruct the helical parameters with a momentum resolution of $\approx 1\%$ ($\Delta p/p$). In general there are 29 hits for a true event and approximately 260 background events for a 30 ns time window with the background from a beam spill of 40 Tp protons. The analysis proceeds as follows.

- Events identified as Compton electrons are rejected by looking for patterns where hits align along a field line. A small number of true hits are also removed by this process, but are later restored after the helix is defined. This step reduces the background by a factor of 2.
- Events are binned in either an x or a y projected view (transverse to the z dimension which is along the field line). For a given view, all three hit combinations are binned with the calorimeter hit to produce sets of 4 hit combinations from which helical fits are obtained. Only combinations that produce momenta $94 \text{ MeV/c} < p < 114 \text{ MeV/c}$ with a pitch angle $41.4^\circ < \theta < 66.4^\circ$ are retained.
- A fifth hit from a different view is then added to the sets. This allows the calculation of the 3 dimensional helical parameters, and from these the circular center of the helix is determined. This center must lie within the target dimensions, and a cut of $-40 < (x,y) < 40 \text{ cm}$ is applied.
- Using the above helical parameters for the surviving 5 hit combinations, each helix is constructed, and the positions of the tracker hits calculated. The residual difference between the calculated and actual hit is determined, and a hit accepted if the absolute value of the residual is $\leq 3 \text{ cm}$. The number of such hits is M.
- The probability that one obtains M hits out of N crossings is estimated by;

$$P = N!/[M!(N-M)!] \epsilon^M (1-\epsilon)^{N-M}.$$

The event is kept if P is greater than a chosen threshold with $\epsilon = 0.95$. After all these cuts are applied, the background is reduced by a total factor of 40.

- The above procedure is then repeated on the restricted set of event points, but here a tracker hit replaces the calorimeter hit. In this step there are on average about 120 four hit and 630 five hit combinations. The helix is then projected to the calorimeter and accepted if it matches the calorimeter position to within 7cm. The analysis assumes a road of only 0.75 cm and a probability of $\epsilon = 0.97$. The background is reduced by another factor of 4-5 by this step.
- Cut hits are then restored and compared to an average helix obtained from the hits that survive the above analysis. Those that match the average helix within ± 1 straw are restored to the list of valid hits. On average 1 real and 2 background hits are added at this stage. This set of hit points is then passes to the CCF analysis.

The CCF analysis uses the drift time and the average helix determined from the first stage analysis. The addition of drift time adds left-right ambiguities on each drift wire (mirrored hits) and increase the number of possible hit points by a factor of 2. The analysis proceeds as follows.

- Chose the first eight straw hits and build 2^8 (256) possible hit combinations corresponding to true and mirror points. The KF forward and backward procedures are applied to these combinations. Only those combinations which satisfy a loose χ^2 cut, $\chi^2 < 30$, are retained (typically about 10 out of the initial 256 combinations). The CCF is applied to each retained combination.
- The true and mirror point choices for the 9th and higher straw hits are taken into account in a combinatorial way, but each time as the number of CCF components reaches the maximum number N, only M components with the best χ^2 are retained.

- The combinatorial procedure is repeated until the number of components reaches again the maximum number N , so in CCF approach the number of components always oscillates between M and N .
- The surviving set of hits (components) reaching the last plane with the best χ^2 is then assumed to represent the track.

In the actual simulation the number of collapsed components was chosen to be 8 and the maximum number of components to be 32. In this case, CCF choses a wrong point only for 4% of the tracker hits if the drift time radius is greater than 0.25 mm.

In summary order the following selection criteria are applied in order to extract the correct particle trajectory with high probability.

- The total number of straw hits is required to be at least 17.
- The pitch angle of the input momentum is required to be at least 45°
- The χ^2 for the trajectory should be less than 40
- The prediction for the fitted trajectory at the point where it intercepts the calorimeter is required to agree with the position of the electron entering the calorimeter within ± 7 cm
- Total electron energy release in the calorimeter is required to be at least 80 MeV
- The difference between the forward (P_{in_f}) and backward (P_{in_b}) reconstructed input momentum has to satisfy the cut $|P_{in_f} - P_{in_b}| < 0.7$ MeV/c
- The difference between the forward (P_{in_f}) and backward (P_{in_b}) reconstructed output momentum has to satisfy the cut $|P_{out_f} - P_{out_b}| < 0.7$ MeV/c
- The difference between the forward reconstructed input and output momentum has to satisfy the cut $-0.05 < P_{in_f} - P_{out_f} < 1.5$ MeV/c

The distribution in the difference between the initial momentum (P_{in_f}) reconstructed by the forward Kalman filter and the generated initial momentum (P_{in}) is shown in Figure ~\ref{fig:pin_difb1} in linear (a) and logarithmic (b) scale for the nominal background rate 600 kHz. According to this distribution the intrinsic tracker resolution is $\sigma = 0.144$ MeV/c if one fits the distribution by a Gaussian in the range -0.3 to 0.7 MeV/c.

We define a minimum momentum to define the lower cut on the signal spectrum, $P_{th} = P_{max} - \Delta$, where $P_{max} = 104.3$ MeV/c is the most probable reconstructed momentum. If $\Delta = 0.7$ MeV/c is chosen then $P_{th} = 103.6$ MeV/c. For the nominal background, the overall reconstruction acceptance is 22.4 % for muon conversion events having momentum above the threshold momentum of 103.6 MeV/c. For double the background rate the acceptance is 20.7 %. In comparison to the results without background, there is a

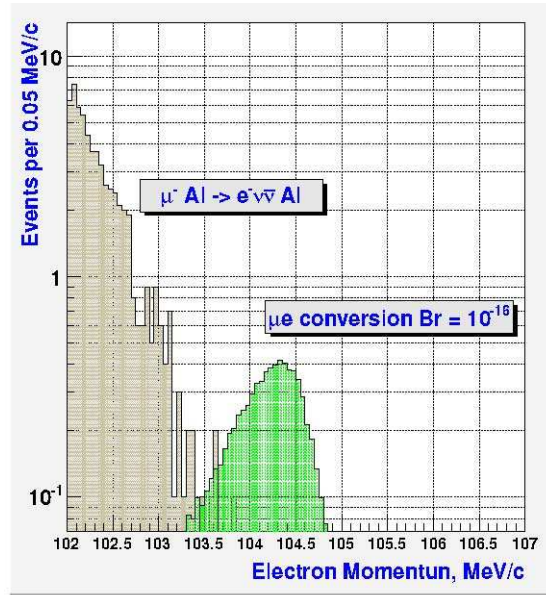


Figure 1.12 Distributions of reconstructed momentum above 100 MeV/c in the presence of the accidental background at rates 600 kHz

1% increase in resolution and a 7.4% and 15 % increase respectively in acceptance for the nominal and high rate background studies. A summary of the critical selection criteria used in the momentum reconstruction is shown in Table ~\ref{table:tab5} for the nominal background rate 600 kHz. The efficiencies are for the selection criteria applied in consecutive order.

In our analysis a reduction of straw efficiency to 97% decreases the overall acceptance for muon conversion events with momentum above threshold momentum to 22%. Inclusion of event loss due cosmic ray vetoes, dead-time, trigger inefficiencies are not included. At the present level of pattern recognition and momentum reconstruction we expect the 0.3 background from DIO events in the range above 103.6 MeV/c compared to 6.5 signal events for $R_{\mu e} = 10^{-16}$.

Further suppression of the background could be obtained if the drift time measurement is complemented by even a rough measurement of the pulse amplitude on the anode wire. This comes about because much of the background is due to heavily ionizing low energy protons that are easily distinguished from the conversion electrons sought in the experiment. An additional and significant further suppression of the background could be achieved if resistive anode wires were used in place of conducting wires. A measurement of the pulse amplitude at both end of the wires gives the hit position along the wire. The price for this additional information is a doubling of the number of the electronics channels. The precision of anode wire measurements can be as high as 1% of the length of the wire. If one assumes a modest precision of for a straw tube of 1 m length, then, at 5σ , the uncertainty along the wire is 5 cm. This gives an additional tenfold suppression of background and leads to improvement in the overall acceptance.

1.2.5 .2 The L-Tracker

Figure 1.3 shows a typical event in the simulation. The number of times the electron helical trajectory turns within the detector region is determined by its pitch angle $\theta_p \equiv \arctan(p_t/p_l)$, and detector length.

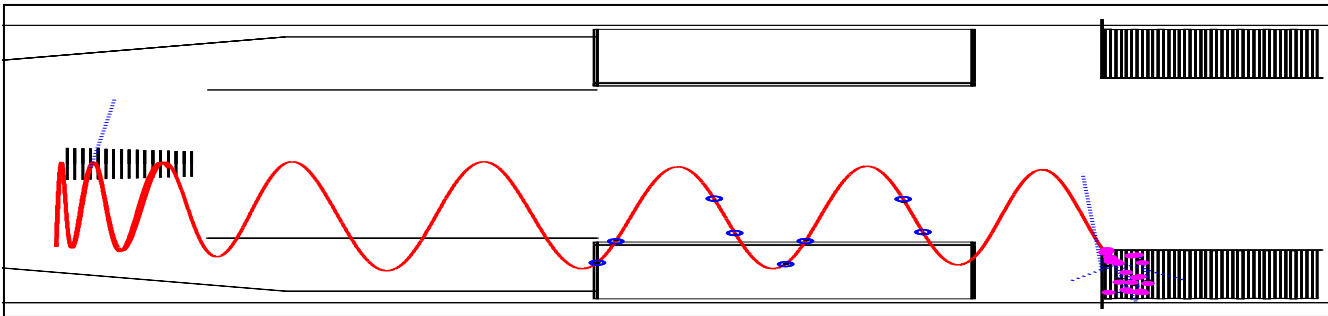


Figure 1.3: Sample conversion electron trajectory in the MECO simulation using GEANT.

The pattern recognition procedure first selects clusters that form circles in the xy (transverse) projection and then matches them with z (axial) clusters to look for good helical tracks. All possible combinations of clusters are allowed. The momentum of the helix track is then determined by a fitting algorithm (*fitter*) that uses a likelihood method described below. The fitter returns the most probable momentum and a corresponding likelihood for this momentum. Since the fitter is very CPU intensive, preliminary selection criteria are used to obtain potentially good circles in the transverse plane and full helices in three dimensions so that the number of possible trajectories analyzed by the fitter is minimized. These criteria are chosen to reduce computing time, while producing a negligible reduction in acceptance for signal events.

Figure 1.4: The left frame shows the cluster number distribution for conversion electrons within the tracking detector acceptance. The right frame is the pitch angle distribution for the same set of events.

Figure 1.4 also shows the distribution in pitch angle for these electrons at the upstream end of the detector. We require that signal events have a measured value of θ_p in the range $45^\circ < \theta_p < 60^\circ$. The lower limit on θ_p eliminates electrons originating in regions with a magnetic field ≥ 2 T, e.g., in the transport solenoid or in the final collimator. It also minimizes backgrounds from beam electrons that scatter in the target, as discussed in Chapter 3, and reduces backgrounds from cosmic rays or events produced in the proton absorber.

The fitter uses the principle of the maximum likelihood method, and determines the most likely momentum of a particle for a helical trajectory. The strategy includes the fact that the trajectory deviates from a helix due to multiple scattering in the detector elements, but individual segments between adjacent hits are helical. The fitter exploits this to determine the trajectory of each segment between detector crossings as a function of the electron momentum p_e , and then calculates a likelihood value $L(p_e)$ for the full trajectory as a function of p_e . This likelihood value is simply the product of the scattering probability at each detector position.

$$L(p_e) = f_2(_2)f_3(_3):::fn_1(_n_1) \quad (9.3)$$

Here n is the total number of hits and $f_i(\theta) d\Omega$ is the probability that the particle scatters into the solid angle $d\Omega$ at θ_i for the detector element where the i th hit was recorded. The parameter $f(\theta)$ has Gaussian

form at small angles with Moliere tails for large angle scattering. It is also possible to incorporate energy loss and the detector spatial resolutions. This is discussed in detail in reference [103].

The most probable value of p_e is the value which maximizes the likelihood. To estimate the error in the value of p_e from the fitter, the distribution in the likelihood vs. p_e in the region of the peak is represented by a Gaussian form. The σ of a fit to this form is denoted σ_{pe} , and it gives a good estimate of the uncertainty in the measured value of p_e . The parameter, σ , and the maximum likelihood value are found to be powerful discriminants against events with badly fit trajectories. The above algorithm is derived assuming the hits which are used are those actually made by the particle track (i.e. no pattern recognition errors). The same algorithm is found to work well even with noise, after applying additional selection criteria, as discussed below.

The following selection criteria are imposed to select the particle trajectories following the track fitting.

1. The value of the likelihood is required to be greater than some threshold value.
2. The scattering angle at each detector element is required to be < 0.08 radian.
3. The fitted uncertainty σ_{pe} is required to be less than 600 keV.
4. The total number of clusters is required to be at least 6 for a 2.4 m detector. This requirement varies with detector length, and it significantly reduces high energy tails in the resolution function, primarily from pattern recognition errors.
5. The fitted trajectory is required to have a cluster at each intersection of the trajectory and a detector element.
6. The projection of the fitted trajectory to the point where it intercepts the electron calorimeter is required to agree with the position of the electron entry into the calorimeter to within 20 cm.
7. The energy of the GEANT primary electron at the entrance of the electron calorimeter is required to be at least 75 MeV.
8. An event is rejected if a lower momentum track is found with a suitably relaxed set of selection criteria. This significantly reduces background from pattern recognition errors with essentially no loss of acceptance for the signal events.

Table 1.2: Pattern recognition results for two different detector lengths and several production windows. A background event is an electron reconstructing with momentum exceeding 103.6 MeV/c and satisfying the selection criteria listed in the preceding section.

Detector length	DIO energy window	Events thrown	Background events
2.4 m	95-100 MeV	5×10^7	0
2.4 m	80-95 MeV	1×10^8	0
2.4 m	75-80 MeV	4×10^7	0
2.0 m	95-100 MeV	4×10^7	2

The intrinsic energy resolution (excluding the effects of energy loss in the target, but including spatial resolution in the tracking detector and the effect of noise) is found to be $\sigma_{\text{RMS}} = 150$ keV. The effect of

energy straggling in the target causes the resolution function to deviate from a Gaussian shape at low energies but does not introduce a high energy tail in the shape of the resolution function. The FWHM of the response function is 900 keV, FWHM. This spectrum is very similar to that of the T-Tracker in figure 1.12 The background to signal ratio can be further reduced below 0.05 with little loss of acceptance. We summarize the efficiencies of the critical selection criteria in Table 1.4. Further suppression of some backgrounds can be obtained by restricting the upper limit on the electron energy. For example, restricting the electron energy to be $103.6 \text{ MeV} < E_e < 105.1 \text{ MeV}$ introduces negligible acceptance loss.

Table 1.3: A summary of the critical selection criteria used in the electron momentum measurement for the MECO detector

Selection criterion	Efficiency
At least 6 hits in tracking detector	0.44
Detected energy above $\sim 103.6 \text{ MeV}$	0.62
Required pitch angle at the detector	0.88
Requirements on fitting quality	0.83
Position match in electron calorimeter	0.97
Overall acceptance	0.19

1.2.6 Backgrounds Induced by Pattern Recognition Errors

We next turn to a discussion of backgrounds due to very high energy tails in the resolution function of the spectrometer. These have been shown to be primarily due to an analysis combining hits from a low energy electron and random accidentals (noise clusters). We refer to this as pattern recognition errors.

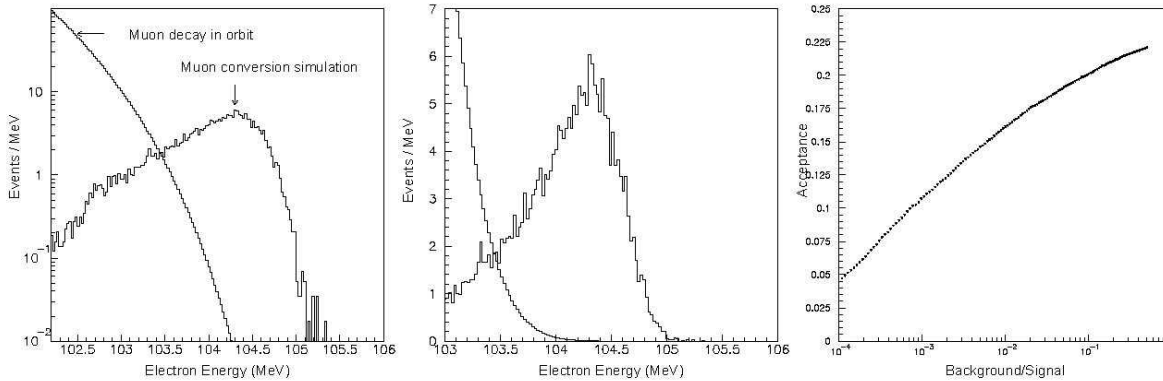


Figure 1.4: The left and center plots are the response function of the detector for 105 MeV electrons generated in the stopping target on log and linear scale respectively. Also shown is the expected DIO background, calculated by convolving the response function with the theoretical DIO distribution. The normalization is to a data taking period of 107 s and $R_{\mu} = 10^{-16}$. The right plot shows a parametric plot of acceptance versus background/signal ratio as the lower limit on the electron energy is varied. These distributions were generated for 105 simulated conversion electrons. The background/signal curve was calculated for a sample of 10^7 events and is essentially identical to that shown.

Table 1.4: A summary of the critical selection criteria used in the electron momentum measurement for the MECO detector

Selection Criterion	Efficiency
At least 6 hits in tracking detector	0.44
Selected energy above ~ 103.6 MeV	0.63
Required pitch angle	0.88
Requirements on fitting quality	0.83
Position match in electron calorimeter	0.97
Overall Acceptance	0.19

While the preceding discussion of backgrounds explicitly includes the possibility of background due to pattern recognition errors, it is limited due to the finite statistics of the calculation, consisting of 10^7 fully simulated events, including noise. The statistical level of this simulation is sufficient to calculate the background arising from DIO electrons with energy above 100 MeV, of which there are $\sim 10^5$ for the total experiment run time. There are many more DIO events below 100 MeV, thus additional calculations are required in order to estimate the expected background level. These calculations are described in detail in reference [45]. Background could, in principle, arise from a variety of sources: multiple scattering, large tails in position resolution, etc. We have found that DIO electrons in this energy range primarily produce potential background by pattern recognition errors [45], but at a level well below the sensitivity of the experiment. We briefly describe those calculations here. In this discussion, we define a background event to be a reconstructed track with momentum above 103.6 MeV. The pattern recognition and fitting code imposes an upper limit of 120 MeV on the reconstructed energy; hence the background is in the interval $103.6 \text{ MeV} < E_e < 120 \text{ MeV}$.

Table 1.5 gives the integrated flux for DIO electrons during the nominal 10^7 s run time of the experiment. The integrated flux rises steeply as the lower energy limit falls, and the energy range that is likely to contribute background can be deduced only by a calculation of the relative likelihood of mis-measured events of different energies.

Table 1.5: The integrated flux of DIO electrons above various energies.

Lower Energy Limit	Total DIO Events
100	1×10^5
95	5×10^6
90	1×10^8
85	1×10^9
80	9×10^9
75	6×10^{10}

Two independent studies were made to determine the number of mis-reconstructed events. Both used GEANT simulations of the detector, but they used different pattern recognition and background rejection strategies. The calculations proceeded by determining the cluster positions of the DIO electrons and superimposing, on average, an additional 24 noise clusters. This is larger than the expected noise rate and allows an efficient determination of the most probable topology of background events.

The more powerful of the two pattern recognition strategies applied the same reconstruction procedure to the DIO events described in the previous L-Tracker section. Results for two different detector lengths and several energy intervals for DIO electron events are given in Table 1.6. A minimum of five clusters was required to form a helix in the 2.0 m detector, and six for the 2.4 m detector.

It was possible to show by direct simulation that for DIO electrons having $E_e > 95$ MeV, the background rate due to reconstruction error is negligible. For lower energy, it is not possible, given available computing power, to generate the full sensitivity of the experiment. Hence, we rely on a study of a sample of events with somewhat relaxed selection criteria in order to infer the properties of events that are likely to cause reconstruction errors. The basic procedure is to relax selection criteria and study the number of noise hits necessary to make background events. It is found that the background events typically use a large number of noise hits, and the high energy component of the resolution function is dominated by events with many noise hits. To study a sample of events with higher probability to produce background, we generate events with higher than expected noise rates, and weight the events appropriately. The specific procedure we use to calculate the expected level of background is to weight each event by suppression factors corresponding to the random probability that a particular event with a certain number of noise hits would occur if we did the simulation with the expected noise rate rather than the increased one.

Table 1.6: Pattern recognition results for two different detector lengths and several production windows. A background event is an electron reconstructing with momentum exceeding 103.6 MeV/c and satisfying the selection criteria listed in the preceding section.

Detector Length	DOI Energy window	Events Thrown	Background
2.4 m	95-100 MeV	5×10^7	0
2.4m	80-95 MeV	1×10^8	0
2.4m	75-80 MeV	4×10^7	0
2.0m	95-100 MeV	4×10^7	2

There are several suppression factors to apply. We have use a mean noise rate three times higher than expected, so there is an event suppression factor of $f_t = (1/3)^{nt}$, where nt is the total number of xy and z noise clusters in the fitted trajectory. Furthermore, the detector plane-helix crossing angle in the transverse plane is determined to high precision so this angle can be inferred locally using the full straw-tube drift time information with a resolution of about 50 mrad. These angles can be compared with the local helix crossing angle to reject clusters if they are not consistent. We estimate that a conservative (high efficiency) cut on the agreement would result in a suppression factor of $f_\theta = (1/8)^{n_{xy}}$, where n_{xy} is the number of xy noise clusters. This is equivalent to the statement that only 1 noise cluster in 8 would have local cluster information consistent with a particle having a well known trajectory. An event suppression factor is taken as the product $f_t \times f_\theta$, and this is then averaged over the background event sample. We denote this average factor as f_s .

For electrons between 95 – 100 MeV, f_s is estimated to be 0.005 for the larger sample of backgrounds satisfying relaxed cuts. Since there is no background found after the final cuts, we calculate P_b , the probability of producing a background per DIO electron if the sample corresponded to one misconstructed background event: $P_b = 0.005/5 \times 10^7 = 10^{-10}$. Multiplying this probability by the total number of DIO electrons in this energy window, we expect 0.0005 misconstructed background events.

Similarly, for electrons between 80 – 95 MeV, f_s is calculated to be 0.00006 for a relaxed sample of background. For this sample, we have $P_b = 0.00006/10^8 = 6 \times 10^{-13}$, and we estimate the background from DIO electrons between 80 – 95 MeV to be $6 \times 10^{-13} \times 9 \times 10^9 = 0.005$. For electrons between 75 – 80 MeV, no background was found even when the fitting criteria were considerably relaxed. Since P_b is smaller for lower energy electrons, we use the value of P_b for 80 – 95 MeV electrons and multiply by the total DIO electron number, as this overestimates the expected background. Taking into account the

triggering efficiency, 0.6 for an 80 MeV electron, we find the misconstructed background from DIO electrons in the energy range 75 – 80 MeV to be $6 \times 10^{-13} \times 0.6 \times 5 \times 10^{10} = 0.02$ events.

In this study, only events with four hits per helical turn were accepted. Other studies have shown that the background level for reconstructed events with three hits per helical turn have approximately the same background level. Summing all backgrounds and accounting for the exponential dependence of the detector rate during the 700 ns detection time, the total expected background is 0.067 events. Doing the same analysis, but assuming a noise rate two times higher than expected results in an expected background of 1 event.

These background events are consistent with a uniform distribution in the energy interval of interest, $103.6 \text{ MeV} < E_e < 120 \text{ MeV}$. Hence, the number of events expected in the signal window size, $103.6 \text{ MeV} < E_e < 105.1 \text{ MeV}$ is about a factor 10 less, or 0.006 events at nominal noise rates.

We further note that this calculation is conservative in a number of ways. First, we have used essentially no energy matching in the calorimeter and only very loose position matching requirements. Second, additional rejection against noise hits can use pulse height information. Protons are heavily ionizing and such hits can be rejected with high probability. Photons cause hits by Compton scattering or pair production, and in both cases the electrons make helical orbits within a drift tube which can also be distinguished by their high anode signals. Third, we have assumed no correlation between xy and z clusters; however, both pulse height and time matching can be used to reject incorrect pairings. Finally, we can reject events with a low momentum track. Currently only low momentum tracks with 4 hits per helical turn are found; rejecting low momentum tracks with 3 hits per turn will further reduce backgrounds.

A more straightforward strategy, employing helical roads, was also used in an independent simulation and analysis of background from DIO events. This algorithm reconstructed events with both 3 and 4 hits per turn and used similar noise rates. It also used energy matching and tighter space matching in the electron calorimeter, but did not use local track angle information. Although it achieved background rejection a few times worse than the strategy described above, it did give another set of direct simulation results on the sensitivity of the background rate to factors like the noise rates, local track angle information, and detector length. The dependence of the expected background level on the noise rate is similar to that of the other analysis, as is the dependence on the energy of the muon DIO electron.

We conclude that if accidental rates are as expected, the muon DIO background from event misreconstruction would be < 1 event with a 2 m detector and is significantly under one event for 2.4 m. This is not a limiting background, however. Making a longer detector provides significant further rejection and insurance against detector accidental rates that are higher than calculated. Some additional background rejection tools not currently used, and provide further rejection possibilities. Based on these studies, we propose a tracking detector length in the range 2.4 – 2.9 m. The actual length will be chosen by balancing construction constraints against the desire for redundancy in event reconstruction.

1.3 Mechanical Construction

The tracking detector and its mounting frame must fit inside the detector solenoid. The inner wall of the solenoid is covered with 5cm of polyethylene blocks to remove neutrons, and the frame and mounting system will require at least 3cm. Table 8.8 provides the radial constraints on the detector.

Table 1.7: Detector solenoid inner radial constraints.

Name	Dimension (m)
Detector Solenoid cryostat nominal inner radius	0.95
Electron trajectory stay-clear radius	0.68
Tracker outer radius	0.70
Typical detector inner radius	0.38
Thickness of polyethylene absorber (estim)	0.05
Clearance	0.03

1.3.1 Construction and Maintenance of the T-Tracker

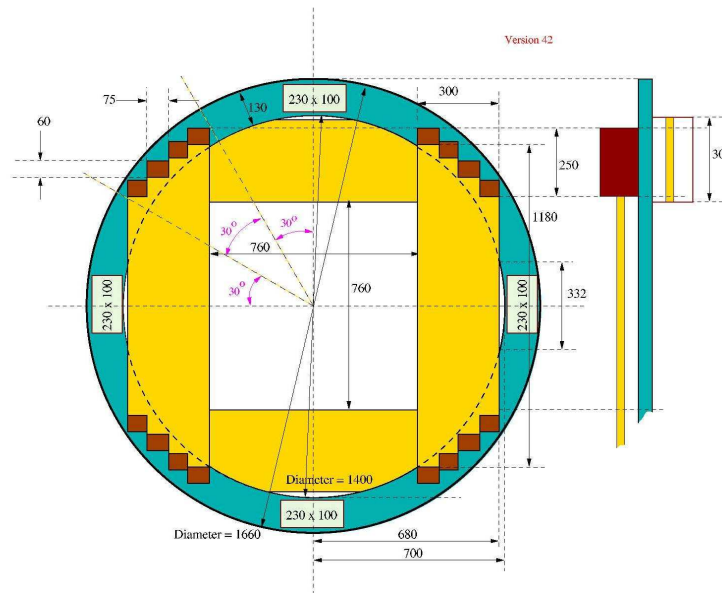


Figure ~\ref{t_tracker} {A cross-section of the MECO T-tracker showing the straw Arrays on the front and back of the straw plane

The present T-Tracker design assumes 5mm diameter conducting straws of 15 μm composed of a double layer of conducting, 7 μm wound Kapton. Although present prototypes use these straws, we may choose to use straws with 25 μm walls (25 μm) if R&D indicates that the thinner walls may develop reliability problems. The gas manifolds, straw feed throughs, and electrical connections are attached to a ring-shaped frame whose radius is larger than the trajectories of the electrons of interest. One straw plane consists of a frame with straw arrays attached to the front and back of the frame. The detector consists of 54 identical planes. Each plane can be individually removed and replaced with a spare as necessary. Three replacement planes will be constructed. Individual planes are mounted on a rigid support structure which is positioned on rails attached to the walls of the cryostat, in order to insert and allow access to the detector.

Individual straws are bonded together in an alignment fixture in units of 15 using a thin layer of casting epoxy. This epoxy easily wicks between the straws, and undergoes minimal shrinkage when set. The ends of each unit of straws are inserted into a tensioning/gas-manifold through an insulating wire clamp, fig{feedthru}. The feed through design is copied from HERA-B. Gas flows through the feed through but the manifold, fig{manifold} is sealed with filling and conducting epoxies to provide a gas seal and a conducting path to ground. The straws in each manifold unit are placed in a holding fixture

and tensioned at approximately 100 g/straw to reduce expansion and sag under gravity. Each tensioned unit is then transferred from the holding fixture to the detector frame, and the procedure repeated, attaching 4 straw units, each of 16 straws, onto the frame. A finished straw array is composed of four 16 straw units producing a trapezoidal array whose straws vary in length from 130 to 70 cm. Four straw arrays are placed on each frame, 2 on one side with 2 on the other side rotated by 90 degrees. Anode wires are strung inside each straw using a needle after orienting each straw array vertically.

Wires are held at high voltage and the conducting straw wall is grounded. One high voltage channel is distributed to the 480 (2 x 4 x 60) wires of each plane. The high voltage for each unit of 16 straws in a manifold has a filter capacitor, 8200 pf, to ground and then passes through a bias resistor of 100 k Ω onto each wire. The signal is extracted through a blocking capacitor of 180 pf. Each wire is fused with a 65ma slow-blow fuse to remove broken wires which short to ground. In the event that a short to ground occurs on a wire, the polarity of the HV is reversed and the normally back-biased diode across the bias resistor allows sufficient current to flow around the resistor through the fuse to open the HV connection. The HV input and signal output from a manifold (16 straws) is constructed on a flex, flat cable on which the components are surface mounted. This cable extends from the preamplifiers outside the gas volume, through a gas seal into the manifold where the HV distribution occurs. There is one HV input line per flex cable, and this line, encapsulated within the Kapton of the flex cable, is insulated against HV discharge/breakdown.

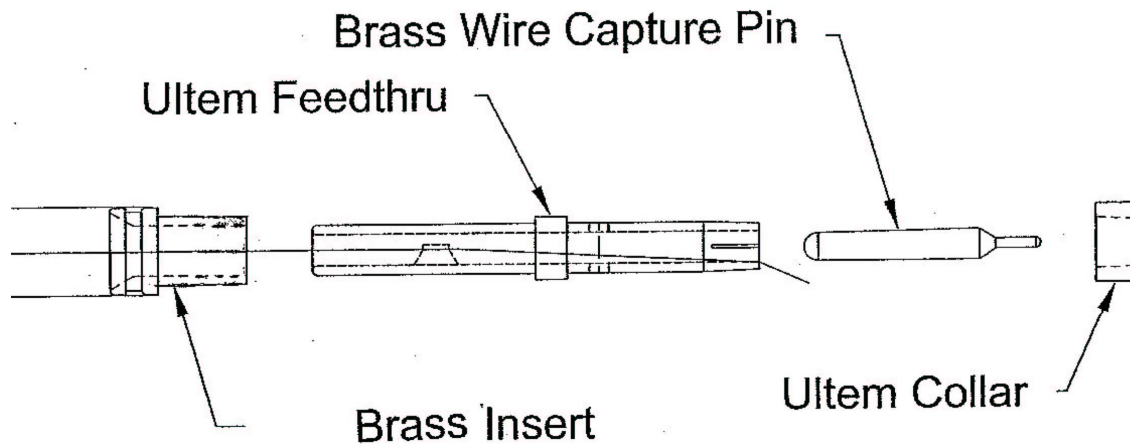
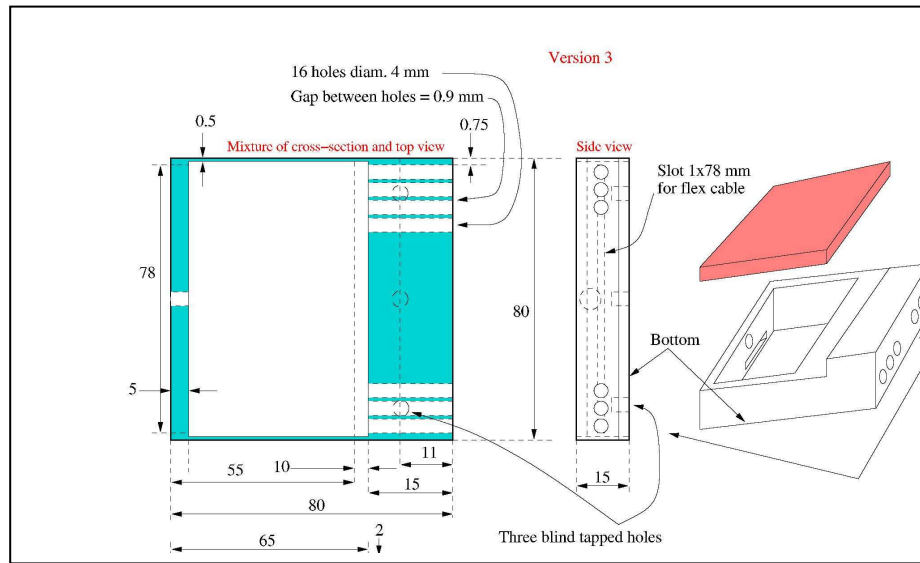


Figure ~\ref{feerthru} {The figure shows a machine drawing of he feed through

The support frame of a straw plane is constructed of two layers of 1/4" Al tooling plate, cut in the shape of a ring. The frame is fabricated from 2 rings of overlapping arcs bonded together by bolts and pins or is welded. It has an outer diameter of 165cm. The inner diameter is notched so that the active area of the straw wires does extend over the frame in order to reduce the number of Compton scattered electrons entering the active region of the straws. The planes are spaced 5.7cm apart making a total detector length of 302 cm, Figure ~\ref{support}.

The description and placement of the readout electronics are discussed below.



Figure{manifold} A schematic drawing of a manifold that will contain and position 15 straws

1.3.2 Construction and maintenance of the L-Tracker

The L-Tracker is 2.6 m long and constructed of 5 mm diameter straw tubes aligned almost parallel to the axial magnetic field. The geometry is described above. Both the octagon plane and the vanes are composed of three layers of nearly axial, close-packed straws~\cite{meco,straws,majewski}. The proposed outer straw layers have 30 μ m thick, carbon-loaded (poly-ether-ether-keytone) PEEK walls, so that the axial coordinate of a hit can be measured by reading the induced charge on capacitively coupled foils placed on both sides of the plane/vanes ~\cite{majewski}. These foils are made of 25 μ m Kapton having 4 mm wide etched copper strips, placed with a 5mm repeat spacing, and are aligned perpendicular to the wire direction. The interior straw layer is constructed of 5mm diameter, 25 μ m thick, metalized Kapton straws. Each plane/vane is bundled into a rigid unit using casting epoxy as described in the T-tracker section , above.

The resistive straws can be made in lengths of 80-100cm, so that three straws are joined to create a straw of 2.6m length. The straw joints will also centrally fix the sense wires and act as hard points to keep the straw plane/vanes aligned. The straws are attached to manifolds at each straw end to provide positioning, gas and electrical distribution, and tension relief. The HV distribution and signal extraction will be similar to that described in the T-Tracker, above. Straws of length 2.4 m require one intermediate support for the anode wire. The straws and wires will be attached to manifolds which provide gas and electrical connections. The manifold and straw mounting fixtures on each end of the straws are made of Aluminum having approximately 2.0 cm width perpendicular to the straws.

A significant feature of the L-tracker is the use of strip readout in order to determine the hit coordinate along the axis of the straw, Figure ~\ref{strips}. These induction strips are etched metalized Kapton 25 μ m thick bundled in 12 strips (6cm) wide. The strips cover the 30 cm width of a vane/plane and have an approximate 35cm long “pigtail” to carry the induced charge to the preamplifiers, Figure ~\ref{induction_strips}. Using strips 4mm wide and interpolating the amplitude of the charge deposited on these strips, we anticipate a position resolution of the charge centroid on the anode wire of substantially better than 300 μ m. A straw resistivity of about 0.5 to 1.0 Mohms/square provides a reasonable signal on the induction pads. Obviously, the higher the resistivity the larger the induction signal, but the longer it takes the collected charge to drain to ground.

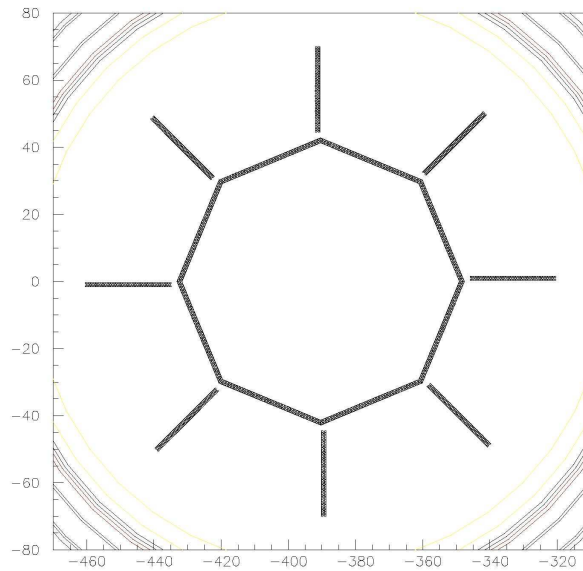
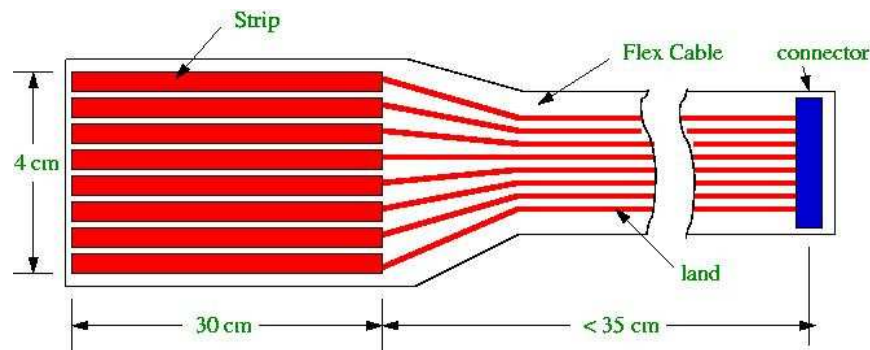


Figure ~\ref{l_tracker} The figure shows a cross section of the L-tracking detector. The vanes and planes are constructed of 3 straw tube layers positioned in a manifold. The detector is 2.6 m long, and the central hole allows DIO electrons and beam particles to pass through the detector to the beam stop without interaction. The magnetic field is approximately perpendicular to the page.



Strip to Front End Board Connection

Position resolution depends on the width of the induced distribution as well as the amount of the induced charge. Both of these depend on the collection time. Position resolution, however, is not an issue as it is more than adequate, (we obtain ~ 300 μm). If the rate becomes extremely high, then signal overlap on the charge strips must be considered. To provide stable operation of the straws, both AC and DC ground are required. It is assumed that the resistive straws are grounded on one side of their cylindrical surface. This makes a significant difference in the width and height of the induced distribution. In the design of the L-tracker, the center straw has cathodes made of metalized Kapton. This automatically provides the AC ground and helps to confine the field lines from the anode charge, reducing the total induced signal, and the width of the induced charge distribution on the cathode strips. The resistive straws will be metalized on the surface next to the conducting straw to bleed the signal current from the cathode. the anode signals. The description and placement of the electronics are described below.

The position resolution constraints are well within what has been demonstrated in a number of experiments. We have assumed a Gaussian position resolution of $200\text{ }\mu\text{m}$ for the drift coordinate and 1.5 mm for the axial coordinate z , for the mean coordinate of a cluster of hits (3 – 4 drift coordinates and two z coordinates). Typical drift resolution in detectors of this type is $160\text{ }\mu\text{m}$ for each drift coordinate [106] and $\sim 10\%$ of the pad width for capacitive strip readout. Operation in a magnetic field will somewhat degrade the performance of the system, but this is not expected to present significant difficulties. In any event, simulations have shown that tails in the position resolution of a few percent which extend out to a straw diameter do not adversely affect the momentum resolution.

Straws similar to these, although somewhat shorter, have been successfully used in BNL Experiment E871 [15]. Low density straw tube systems of 2.7 m , 2.6 m , and 2.4 m have been successfully built and tested by several groups [104], and readout of induction pads through resistive straw cathodes has been demonstrated [105].

1.4 Deformation of Straw Tubes

Deformation of the straws when loaded by gas pressure and wire tension has been investigated. If treated as a cylinder, the internal gas pressure results in an outward force of $\sim 2.0\text{ N}$ per straw, and this exceeds the expected wire tension of $\sim 0.6\text{ N}$. At issue is the extent to which the straw deforms due to this loading. It is noted that long straws are generally placed under an outward tension of about 1.8 N in order to align them before wiring. We tested the fractional stretch of a straw by increasing the pressure in a sealed straw with one end fixed and the other free. The typical fractional change in length is 0.04% for one atmosphere overpressure. Of more concern is the change in straw dimensions as a function of humidity. The CKM collaboration found that straws of similar diameter experienced dimensional changes as given in Table {ckm}. In this table RH is the relative humidity. One notes that the expansion due to 1 At pressure is only about 40% of the expansion that would occur for an externally applied force of the same magnitude. We observe similar expansions in our measurements in addition we have observed creep at various tensions on the order of $\Delta L/L \approx 1.6 \times 10^{-4}$ over the period of 7 days.

Table {ckm} Linear expansion data measured of a kapton straw of 1 m length and 5.1 mm in diameter.

Linear Expansion Coefficient	$5.1\text{ }\mu\text{m/g}$
Linear Thermal Expansion	$9.9\text{ }\mu\text{m/F}^\circ$
Linear Humidity Expansion	$12.0\text{ }\mu\text{m}/\% \text{RH}$
Linear Pressure Expansion (15 Psi)	$380\text{ }\mu\text{m}$
Radial Expansion (Psi)	$6.7\text{ }\mu\text{m}$

In order to stabilize the mechanical properties of the straws, we are presently attaching thin carbon wires lengthwise along the straw surface. The results of these studies are forth coming.

In addition to the above study we have begun a study using computer simulation calibrated by the mechanical moduli that we are measuring. We are therefore collecting data by horizontally suspending straws and prototype planes with the system placed under pressure and tension, and the sag measured at various points along the horizontal-axis. We fit this data to the model to extract the flexural rigidity of the system. Flexural rigidity is the force-couple required to bend a specimen to its unit radius of curvature and is expressed in dyne-cm units 10^{-9} J .

Calculation of the flexural-rigidity, D , of a plate requires the use of the theory of elasticity\cite{plate_theory}. The applied forces to the plane are gravity and tension.

$$M = -D \frac{d^2 \epsilon}{dx^2};$$

where M is the bending moment, and x is the horizontal distance. There is also a twisting moment which is ignored in this analysis. Quantitatively, the flexural-rigidity is given by;

$$D = \frac{Eh^3}{12(1 - \nu^2)}.$$

In this expression, E is Young's modulus and ν is Poisson's ratio. To explicitly calculate the flexural-rigidity of a rectangular plate, it is necessary to first solve the equation of a surface of deflection. This is a fourth-order partial differential equation which is obtained by taking an infinitesimal element, $dx \times dy$ of the surface and assuming that no body or tangential forces act on the faces of the plate. The load acting on the element, gravity, is $g \, dx \, dy$. The normal forces are N_x and N_y while $N_{xy} = N_{yx}$ represents the shearing forces.

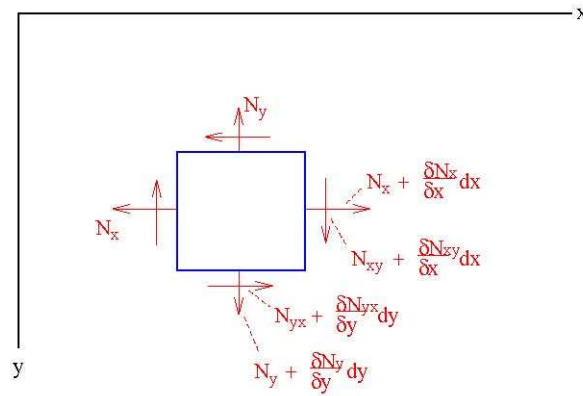


Figure 1.16 An infinitesimal element of surface of deflection illustrating all the possible forces that could be applied to it in two-dimensions

In this analysis, there are no shearing forces, and the normal force, N_x , applied as a uniform tension, acts parallel to the x -direction. There is a uniform lateral load (weight of prototype), q . The equation for the deflection is then;

$$\frac{\partial^4 \omega}{\partial x^4} + 2 \frac{\partial^4 \omega}{\partial x^2 \partial y^2} + \frac{\partial^4 \omega}{\partial y^4} = \frac{1}{D} [q + N_x \frac{\partial^2 \omega}{\partial x^2} + N_y \frac{\partial^2 \omega}{\partial y^2} + 2 N_{xy} \frac{\partial^2 \omega}{\partial x \partial y}]$$

This equation and its boundary conditions, $\omega(x \pm a/2) = 0$, will be satisfied by taking the deflection, ω , in the form of the series

$$\omega = \frac{16q}{D\pi^6} \sum_{m=1}^{\infty} \frac{1}{m \left[\frac{m^4}{a^4} + \frac{N_x m^2}{D\pi^2 a} \right]} \left[1 + \cos\left(\frac{m\pi x}{a}\right) \right]$$

$$D = \frac{E h^3}{12(1 - \nu^2)}$$

Measurements of the deflection, ω , as a function of x , allows the extraction of D and therefore, E and ν .

1.5 Wire and Straw Support

Several wire support designs have been studied. One design uses injection molded plastic [107]. In this design the overall form is a cylinder, 3.95 mm in diameter, and 4 mm long. The central portion which grips the wire is molded as a blank disk, and connected to the wall by three spokes. In use the wires have been measured to center within 40 μm . Its weight in the MECO application (where the straw diameter is 5 mm) is estimated to be 0.07 g, compared with 1.5 g for a three meter long straw. In addition there are the designs of [108]. One of these consisted of a plastic cylinder 7.7 mm long with a helical groove. The groove was one cylinder radius plus one wire radius deep, had a circular shape at the bottom, and made one complete turn around the cylinder. The mass of one such piece is about 0.15 g. The other design was called the “double-V”, and was made of two pieces each with a V-shaped slot. The apex of each V was on the center of the straw, with one rotated 180 degrees with respect to the other. We intend to evaluate these different designs for use in MECO, expecting that at least one of them will meet our needs. wire stability can be estimated using the relation

$$T_c > [1/2 \pi \epsilon] (V C L / \pi R)$$

with T the tension of the wire, V the voltage, C the capacitance per unit length, L the wire length, and R the straw radius. The straws should be tensioned at about 80 g. A Kapton straw stretches about 0.06% per 100 g of tension. wires with 25 μm diameter can be tensioned to 80 g (0.78 N).

1.5 Straw Operation in Vacuum

We tested the leak rate of straws under vacuum. Our tracking simulations have assumed we would use straws similar to those used in E871, which are made of two layers of Kapton, each 0.0005 in thick, spiral wound with a half strip overlap. The inner layer has ~ 1000 Angstroms of copper deposited on the interior. We tested the leak rate of both the bulk straw material and the end fittings by measuring the rate of rise of pressure in an evacuated tube containing sample straws with one atmosphere pressure. The rise of the chamber pressure was measured as a function of time after the pump valve was closed. The rise decreased with initial pumping time, indicating it was due to out-gassing of the exterior of the straw. The residual rise after 5 days of pumping corresponded to a leak rate of $\sim 2 \times 10^{-8}$ l/min/m for the bulk straw, and a leak rate of $\sim 3 \times 10^{-9}$ l/min per end. These leak rates, when scaled to the full spectrometer, are well within modest pumping rates. Furthermore, straw tubes have been operated in vacuum in a

previous experiment [110, 111]. We have also constructed prototype low-mass gas and electrical manifolds in which a fraction of a “vane” module has been assembled.

1.6 Pad Readout

A significant feature of the straw chamber spectrometer is the use of pad readout to determine the coordinate along the straw. This technique has been previously demonstrated [105]. Straws are constructed of carbon loaded Kapton, which have a resistivity between 500 k Ω and 1 M Ω per square. A resistive cathode allows an electrical signal to be induced on copper pads deposited on a thin film of Kapton placed outside and perpendicular to the straw assembly. We envision one pad layer on each side of a three-layer straw plane. Using strips 5 mm wide and interpolating the amplitude of the charge deposited on these pads, we anticipate a position resolution of the charge centroid on the anode wire of ≤ 1 mm. In our detector simulations, we used a resolution $\delta = 1.5$ mm, which is significantly larger than what is routinely possible. The development of the straw system and its readout electronics requires significant R&D effort before engineering design can begin.

The total induced signal on the sum of the cathode strips is less than 1/2 the amplitude of the anode charge, and this signal is then distributed over at least 5 strips such that the central strip contains $\approx 40\%$, and the two strips to either side of the central strip $\approx 25\%$ of the imaged charge. Thus the amplitude of this induced charge (and the noise on these strips) requires a longer integration time than for

1.7 Choice of Straw Resistivity

To determine the axial hit position, the collected anode charge must be imaged and read from cathode strips placed perpendicular to the straws. The straws must be constructed of resistive material with reasonably thin walls (~ 25 μm). Resistive Kapton can be supplied in thicknesses ≥ 19 μm and with standard resistivities $0.5 - 1.0 \times 10^6$ Ω/square .

We have studied the expected signal from a cathode pad using an equivalent circuit model as shown in **Error! Reference source not found.** The model has 640 nodes. The center node, m , is injected with a current signal having 5 ns rise and 15 ns fall times. The strip signal is shown as a function of the cathode resistivity (a 640 k Ω value of R_{cath} is equivalent to 1 M Ω per square). The integrated charge on the strips, m , $m+1$, etc. is consistent with a static image model [112, 113, 114], indicating that ratio of charge on the $m \pm 1$ strips to the central charge is approximately 20%. The induced signal for various values of R_{cath} is shown in **Error! Reference source not found.** We conclude that a cathode resistivity between 0.5 – 1.0 M Ω per square provides a sufficiently transparent foil for the straws.

The recharge time following the particle ash associated with the beam microstructure also limits the straw resistance. This has been studied using the circuit model above. We find that we must ground the semi-circular region of the straw opposite to the induction stripes to reduce the total cathode resistance. If this is not done the straws cannot recover from the beam ash.

The minimum thickness Kapton film made by Du Pont is 0.3 mil (“H” type). The “XC” type of 0.75 mil thickness can be carbon loaded. It is apparently not possible to manufacture resistive Kapton thinner than 0.75 mil, however it may be possible to make straws from combining an inner layer of “XC” type Kapton with an outer layer of “H” type Kapton, resulting in a total thickness of 1 mil (25 μm). Mechanical properties of this structure must be studied.

The resistivity of standard “XC” Kapton is 5×10^5 ohm/square and costs \$3.70 per square foot, with a minimum order of \$3000. To custom produce layers 0.75 mil thick with lower resistivity, the minimum order increases to 20,000 square feet. The accuracy of the resistivity of standard material is ± 1 order of magnitude. The material is 30% more expensive if the error in resistivity improved by a factor of 3.

1.8 Drift Gas

Because of the expected rates, and particularly the required recovery time of the detector after the beam-ash, we intend to use a fast drift gas such as 80% CF₄ with 20% isobutane [115]. In addition, we plan to limit the gas gain to approximately 5×10^4 . Although this will also limit the spatial resolution of hits, our requirements of $\delta = 200 \mu\text{m}$ are easily obtained. magnetic fields up to 2 T in CF₄/isobutane have been studied [108] in the laboratory. At 1 T, the Lorenz angle is $\approx 45^\circ$ at 1 keV/cm and $\approx 20^\circ$ at 4 keV/cm. The drift velocity in the drift direction varies from $70 \mu\text{m/ns}$ at 1 keV/cm to $120 \mu\text{m/ns}$ at 4 keV/cm. The magnetic field in the MECO detector region is constant along magnet axis, 1 T, but the E field varies as a function of radial distance r . We expect the drift velocity along the radial direction to be $50 \mu\text{m/ns}$ at 1 keV/cm and $110 \mu\text{m/ns}$ at 4 keV/cm.

1.9 Readout Electronics

The readout electronics are designed to work with either the T-Tracker or the L-Tracker. In particular the electronics will be used to read both the anode wires of the T- and L-trackers as well as the cathode strips of the L-Tracker, albeit with a slight change in integration constants to better match the different components. In general, the number of readout channels is large, power consumption is severely restricted, and cabling and the electronic footprint are constrained by space limitations. Therefore the readout architecture will take advantage of modern integrated circuits technology, placing a multi-channel IC at the front end of the detector to read, digitize, and buffer the signal. The advantages of a fully digitized, pipelined, dead-timeless front-end, have been implemented in several modern data acquisition, DAQ, systems [4]. The design for the MECO tracker uses an update of successful ASIC designs. From particle flux calculations, including a neutron uence of $3 \times 10^{11} \text{ yr/cm}^2$, we expect that “rad-hard” production processes will not be necessary. Thus MECO can use standard CMOS technology.

Because of space limitations we assume a preamplifier placed on the detector plane near the anode wires and cathode strips. These preamplifiers then feed an amplifier/discriminator placed on a digitizing board controlled through a local bus by a readout controller. Our prototypes use an amplifier-shaper-discriminator (ASD) chip, which was designed for the Atlas thin gap chamber [3]. The threshold can be set remotely by computer and it has both timing and analog outputs. Each ASD IC has 4 independent channels. This ASD must be replaced because it is too old to be reproduced in modern foundries, and in any event pulse pile-up and dynamic range due to highly ionizing, low energy proton backgrounds must be addressed. For example, it is expected that there is a factor of 25 difference in ionization between the electrons of interest and these low energy protons.

1.9.1 Front End ICs

We propose to develop a common design for an Amplifier Shaper Discriminator (ASD) that could serve the T/L-tracker anode wires, cathode strips for L-tracker, and perhaps the APDs of the electron calorimeter. The ASD should have analog (linear) outputs as well as digital (discriminated) outputs. A calibration feature is needed to inject signals of a known size to individual channels. Finally, the power dissipation should be less than about 50mW per channel since these ICs will be used in the vacuum.

The preamp must be able to handle bipolar input signals since the anode wires will provide negative pulses and cathode strips and APDs will provide positive pulses. To some extent any amplifier will amplify signals of either polarity however usually one polarity is favored by having a much larger linear dynamic range. Some characteristics of the signal sources are given in the table below.

Characteristic	Anode Wire	Cathode Strip	APD
Input Amplitude	2 – 60 fC	3fC	16-25 fC
Capacitance	30 pf	100pf	150pf

An example of an existing ASIC which has true bipolar input capability, i.e. a large linear dynamic range for both polarities, is the CARIOCA chip [1] developed for the Multiwire Proportional Chambers of the LHCb muon system.

In the event that charge division along the anode wires is used in the T-tracker design the preamp input impedance should be much lower than the resistance of the wire, perhaps $Z_{in} \sim$ few tens of ohms. On the other hand in the L-tracker design the anode wires are much longer and comprise one conductor of a complicated transmission line structure. The preamplifier impedance should then be adjusted to provide maximal damping to potentially resonant behavior. In the usual IC implementation of a transimpedance amplifier the input impedance can be conveniently adjusted by simply changing the biasing current of the input transistor. Furthermore, to optimize noise vs speed trade-off for cathode pad readout of the L-tracker and/or APD readout of the electron calorimeter it may be desirable (in the case of BJT technology) to adjust the bias of the input transistor. Therefore it is desirable for the preamplifier to incorporate a means of adjusting the input impedance or the biasing of the input transistor. This technique has been used in the amplifier ASIC [2] of the BaBar drift chamber.

The equivalent noise charge should be less than $\sim 0.5\text{fC}$ ($\sim 3000e$) in both the tracker applications as well as its potential application in the APD calorimeter readout. Achieving this will depend somewhat on the shaping or filtering employed in the entire processing chain. To maintain maximal flexibility only bandwidth-limiting filtering will be required, e.g. $\sim 10\text{ns}$ peaking time for a delta-fn input, in the ASD. Other shaping can occur in subsequent circuitry. For example the ion-tail-cancellation for tracker signals can be performed on the digitized waveform data [3]. This digitally filtered waveform could then be used offline to correct the timing of the digital output if necessary. Similarly the risetime of the amplified APD signals can be stretched by a linear circuit preceding its digitizer.

Due to the beam flash, low energy protons and APD-nuclear-counter-effect there will be frequent signals many times ($\sim 25X$) larger than the average electron signal. The preamplifier need not be linear for this extended range; it is acceptable for it to limit somewhere beyond the signal ranges given in the table above. However, it is important that the preamplifier recover from an over-range signal quickly, in

less than $\sim 50\text{ns}$ since the active part of the spill is only 600ns in length. Response to overload signals is often not specified in existing ASIC designs but it is of crucial importance here.

Each channel of the ASD should have a linear output to drive subsequent circuitry. The tracker electronics will have the ASD and waveform digitizer either on the same PC board or separated by a short flex cable. The linear output should be a differential "current-steering" type (like LVDS) to avoid ground bounce and other common-mode noise/instabilities. On the other hand the calorimeter amplifier must send its signal outside the vacuum, presumably on a low impedance cable, to the digitizer and trigger. In this case the calorimeter amplifier will need a cable driver, employing COTS ICs, on the PC board.

Each channel should have a discriminated (digital-LVDS) output with duration corresponding to time-over-threshold, perhaps modified by hysteresis. The threshold should be applicable either chip-wide or on a channel-by-channel basis. In the former case AC coupling with a baseline restorer to reduce threshold dispersion might be needed. However the response of a baseline restorer to over-range signals (i.e. possible overshoot) must be thoroughly investigated before we adopt that approach.

The ASD should have 4-8 channels per package. Probably a 4-channel package is a better choice for decoupling and thermal considerations.

Our plan is first to investigate whether any existing amplifier ASICs which have any features in common with what we need can be modified to meet our requirements. For example the ASICs described in [1] and [2] each have some features we need. Modification of an existing design or development of a new design will be done by a EE graduate student under the guidance of an EE faculty at the UVa engineering school and UVa physicists. Testing of the produced chips will be done by a technician under the direction of UVa physicists.

All components are mounted directly on the support structure of the tracker and are actively cooled by chilled coolant owing through pipes attached to this structure. The 4 preamplifier ICs in units of 8 channels each are mounted onto a daughter board that connects with 4 digitizing ICs (8 channels each) channels to compose a building block. This board covers 16 cm of readout (32 channels of either straws or strips). The 4 building blocks are mounted on a mother board which contains the local buffers and local readout control. There are 16 MB per vane reading the strips of one vane and one octagonal plane. It requires 3 MB to read the anodes.

The front end readout electronics for the straw tubes and strips can be similar. What is needed is a preamplifier that feeds both a digital and an analog circuit. Of course each type of preamplifier must appropriately match the two different signal inputs to the output circuitry. The digital circuit consists of a discriminator providing a fast time signal, $\sim 1\text{ ns}$, and then generates a vernier signal based on a delay locked loop which is injected into a clocked pipeline measuring the time difference between the trigger and the fast time signal. The analog circuit feeds a flash ADC which is also clocked into a digital pipeline. The ADC provides an integrated time-slice, $\sim 60\text{ ns}$ wide. A coincidence between the signal from a straw and the strip provides the address of the correlated components which are to be read for each hit, and an output for that channel is inserted into a local buffer when a trigger gate is present.

The pipelines are clocked at frequencies between 15 – 20 MHz, and will be about $1\text{ }\mu\text{s}$ deep. In order to obtain more precise timing information, for example to make drift time corrections, the vernier allows

interpolation to 1 ns between the clocked intervals. We note that the drift time in the straws will be of order 50 ns, so one clock pulse will encompass the drift time, and the vernier clock would run at approximately 60 MHz based on a 64 tap delay locked loop. Each trigger is numbered and used as a time stamp (trigger ID) in order to reconstruct the event, and to provide a local time, modulo 60 ns. Between micro-spills, the local buffers are flushed.

The Anode Preamplifier (AP) IC must match the impedance, noise and rate requirements of the anode wires. It supplies both a fast timing and a shaped amplitude signal to the digitizers. Several chips are available, but a modern design having both timing and amplitude signals does not exist. There is some development work underway for other detectors and it may be advantageous for MECO to join this effort. Typical power dissipation is about 10 – 20 mW/channel.

The Pad Preamplifier IC (PP) is similar to the AP but requires lower noise and must integrate over a longer time window. Given the pitch of the strips, the channel number in one IC should be ≤ 8 . Unfortunately there are no ICs which match our specifications. For example, the preamp ICs used for the PHENIX TEC have similar specifications but have no timing output. It may be possible to modify this chip by removing one amplitude output and adding a discriminator. However the chip is designed in 0.8 CMOS technology and is no longer supported by the foundry.

Digitizer

Most of the power in any readout system is expended on bus interfaces and impedance matching connections. These factors can be deleted or reduced in a front-end application specific, ASICs. For example, an analysis of power consumption indicates that to drive an AT signal out of the detector vacuum enclosure requires at least 150mW/channel, and in addition, has the difficulty of making tens of thousands of vacuum feed-through connections. An A/D ASIC consumes 31.3mW /channel and can have only ten or twenty readout cables. We have identified an A/D ASIC, which provides digitized signals of both the analog waveform and threshold time signals [8]. This **Electronic Front-end Amplitude and Timing, ASIC, (*Elefant*) is used in the BABAR experiment at the Stanford Linear Accelerator. It has 8, parallel channels of flash ADC and 8 channels of *delay lock loop* (DLL) TDC, and a latency buffer to temporarily store the digitized data and send selected events to an event buffer at the presentation of the first level trigger, L1. The L1 trigger is the external physics trigger that initiates the readout sequence, and occurs at some time latency after the detector signals are stored. The chip can handle high single rates, and has low power (250mW/ 8-channel).**

Unfortunately, *Elefant* was designed 7 years ago [9], and although successfully used for drift chamber readout, was fabricated in a 0.8 μ m, 3-metal, 2-poly, CMOS process that is obsolete. In addition its 5V I/O is difficult to interface to modern FPGA designs, and its clock speed is insufficient for our purposes. However we can take advantage of new CMOS technology by rescaling this chip to match our requirements. The design has been proved by prototyping. The block diagram of the AT digitizing system is shown in Fig ~\ref{architecture} and has been successfully prototyped and tested using the older *Elefant* ASIC.

All function blocks are built around the latency buffer, which temporarily stores the signal information before the trigger decision is made. The latency time is equal to the depth of the buffer times the clock cycle. This must be more than the time delay to make the trigger decision. In the present design this is 4.3 us for a clock frequency of 60 MHz. The sample rate of the ADC and the accuracy of the timing are also related to the clock rate.

The A to D block processes 8 data channels in parallel, and the ADC and TDC encodes with 10 bit accuracy. Since the latency buffer alternatively stores the ADC and TDC data, two characteristic bits

are used. Thus in the present design, the chip has a 64 bit bus-width. Two dual port SRAMs, (SRAM1 for data storage as an event buffer and SRAM2 for time stamp and hit map storage) are fed by the latency buffer. Upon an L1 trigger, a pre-defined record length (8, 16, or 32 of data words each containing 64-88 bits) are moved from the latencybuffer into SRAM1, and a corresponding time stamp is stored into SRAM2. When the data are moved, an 8 bit hit-map is formed, in which a bit is set when at least one TDC hit is recorded in the corresponding channel. The data in these SRAMs are then sequentially moved to the next buffer level under control of a FPGA, which uses the hit-map for zero suppression.

A unique component of the design is the hit map, which provides hit occupancy for use in the generation of the event trigger. An external trigger logic circuit can then select appropriate data to be read from the latency buffer. In the low occupancy situation, the system can be self-triggered where all hits can be read into the local bus. In high occupancy situations, such as MECO, an external trigger can be constructed by coincidence with additional information so that only a filtered set of events are recorded, thus increasing the bandwidth for this subclass of events.

4.1 T-Tracker Readout

Signals from the anodes are cabled through a preamplifier to amplifiers on the front-end/digitizing, FEB, boards. The FEB process 32 channels/board and contains a four 8 channel digitizing ASICs which provides a digitized timing output (16 bits) and a digitized waveform containing 15 time slices each containing 16 bits (total of 16×16 bits) for each channel. This information is pipelined for latency, gated, readout zero suppressed, buffered, labeled with a trigger stamp, and transmitted on command to a higher processing level. Each FEB is connected via a backplane to a readout controller, ROC, whose FPGA memory and commands can be programmed interactively. A ROC controls approximately 6 FEB and there are 72 ROC in the detector. Each ROC is connected through a local bus (16 bits) to a readout sequencer. Each sequencer controls 4 ROC and uploads data and downloads communication via a serial bus link. There are 18 sequencers which then transmit data and information serially on parallel lines via an optical link through the vacuum wall to a memory in an external memory/processor. All modules are in a shielded enclosure. Data transfer rates of a few hundred Mb/s are anticipated.

Table {T-tracker_ro} gives the channel readout organization for the T-Tracker. All of the modules and cables are contained in a shielded enclosure.

4.2 Data Rates for the T-Tracker

Data rates are based on the single hit structure and background rates expected in the T-Tracker. If the background rate is 0.5×10^6 and the trigger gate is 167 ns (10 clock ticks), then for 12960 wires, 1082 accidental events/trigger are registered. From simulation, a true signal involves 35 channels, so the total number of channels containing data is $(35 + 1082) \approx 1120$. There are 20 words/trigger and 16 bits/word which results in 357 kbits/trigger. For 1000 triggers/s the data to be transferred is 357 Mb/s. This is transferred over 18 serial optical lines.

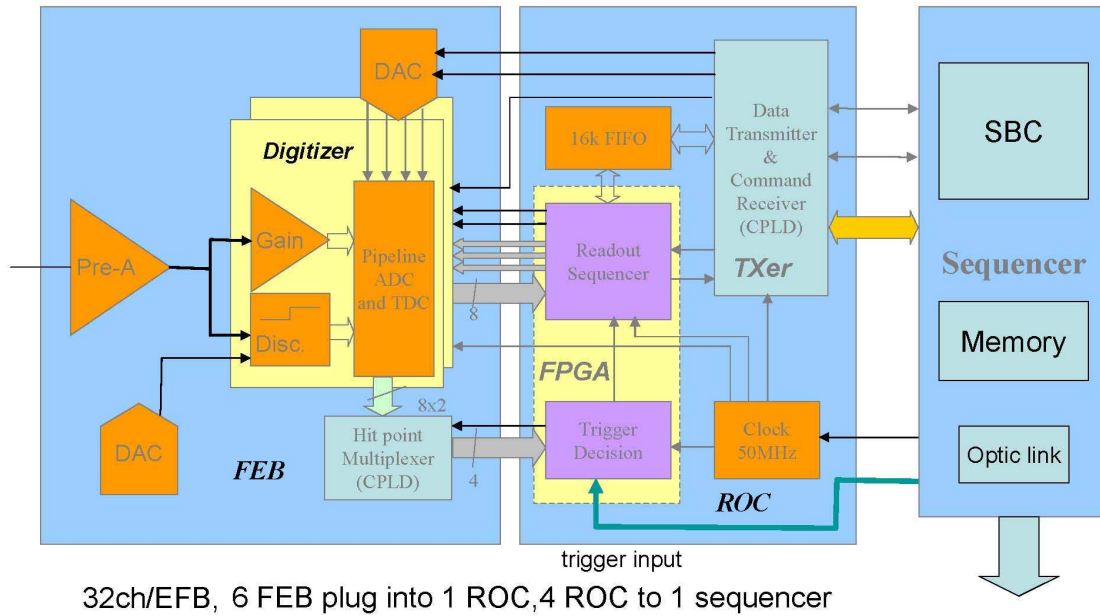


Figure ~\ref{architecture} A block diagram of the front end architecture for the readout electronics. The figure shows the preamplifier board (ASD), the Elephant digitizer board, and the readout controller.

Table ~\ref{T-tracker_ro} Channel Readout organization for the T-Tracker

	Manifold	Plane	Detector	Channel/straw
Number	16	240	12,960	1
FEB	1/2	7.5	405	
ROC	1/12	1.25	67.5	

4.3 Longitudinal Tracker Readout

Readout for the L-Tracker is organized in a way similar to that of the T-Tracker. Signals from the anodes and induction strips are cabled to the preamps mounted along the outer radius of each vane. These feed front-end/digitizing boards. The digitizing boards are connected via a backplane to ROCs and each ROC is connected to a readout sequencer. All modules are in a shielded enclosure. The readout is organized along a vane as shown in Figure ~\ref{l-track_ro}.

For the L-Tracker, 11 FEB and 2 ROC modules are required to read the anodes of a vane-plane (344 wires). To read the cathodes strips of a vane-plane (2 x 1040) requires 66 FEB, 11 ROC, and 3 sequencers. There are 8 vane-plane readouts per detector so 528 FEB, 88 ROC, and 24 sequencers are required. Table {L-tracker_ro} gives the channel organization for the L-Tracker.

Table {L-tracker_ro} The table gives the readout organization fo the L-Tracker

Channels/ vane-plane		FEB	ROC	Sequencer
Anodes	344	11	3	0.75
Induction Strip	2080	66	11	2.75

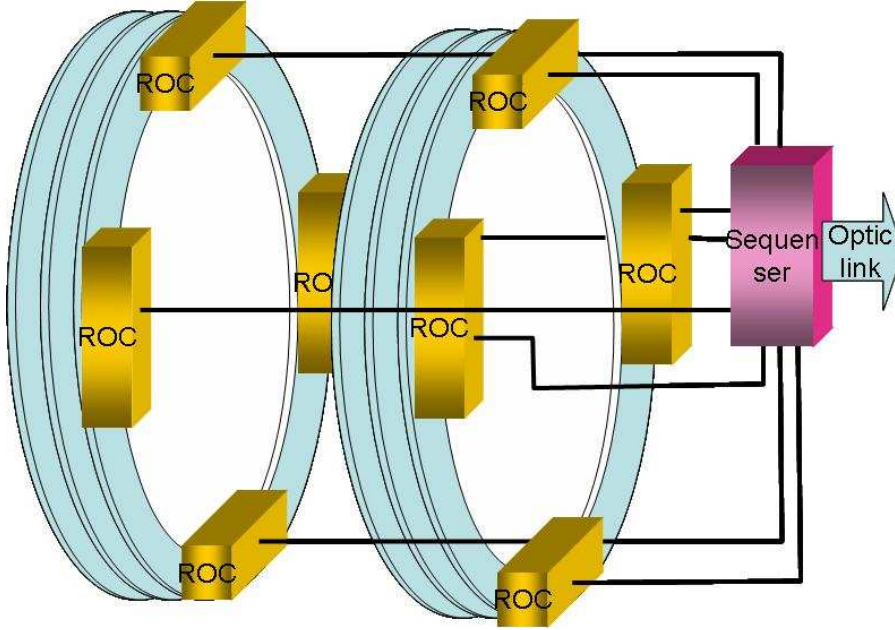


Figure ~\ref{t-track-ro} The figure shows a schematic view of the placement of the readout electronics for the T-Tracker. The ROC are connected by a local bus to a sequencer at the downstream of the detector which sends data serially out of the vacuum to the data acquisition system an communicates with the DAC by fast and slow controls.

The MECO electronics system consists of four major components: 1) the tracking detector,2) the calorimeter front-end, 3) the trigger, and 4) the data acquisition processors. We discuss only the tracking detector in this section.

The MECO baseline tracking detector is a 2.6 m long, octagonal cylinder with 8 vanes. The total number of readout channels (see **Error! Reference source not found.**) is approximately 2880 straw anode wires and approximately 16640 analog strips. The straw wires are read at the downstream end of the detector and the strips above and along each detector vane. All channels will have both ADC and TDC information. Data rates for acquisition are based on the following assumptions.

1. The singles count rate per straw is 500 kHz during the detector-active period (700 ns).
2. The total number of hits during the beam ash is ~5 per straw.
3. The position resolution of the straw is 200 μm for the transverse dimensions, and 1.5 mm for the parallel dimension.

4. The trigger rate is 1 kHz.

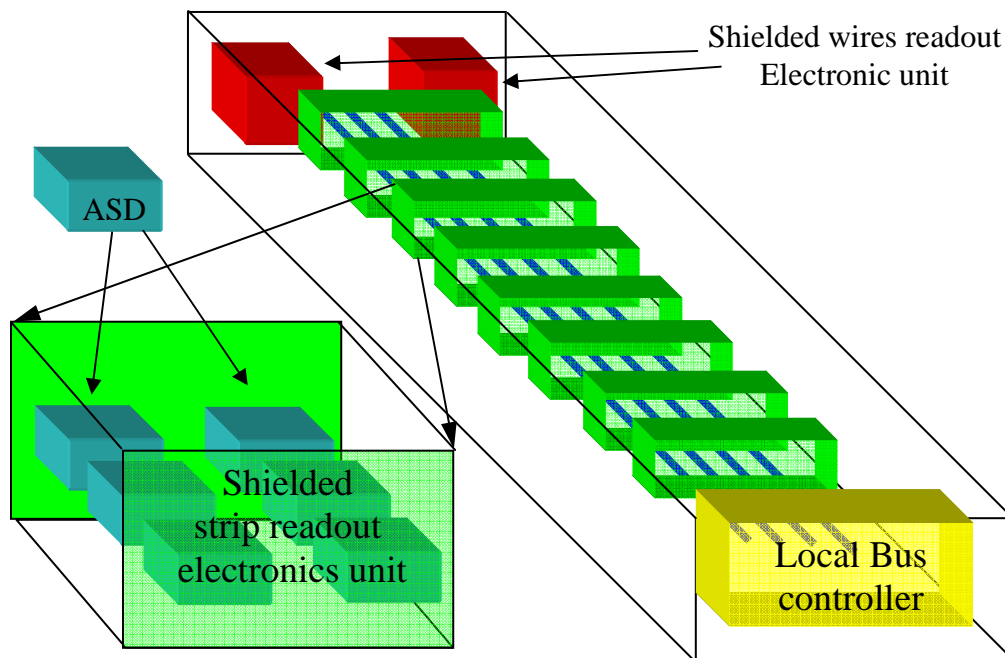


Figure ~\ref{l-track-ro} The figure is a schematic of the readout architecture of a vane/plane showing the local ROC units, the local bus and the local bus controller/sequencer which serially transfers the digitized data through the vacuum wall.

1.10 DAQ Architecture

In order to develop a readout architecture, one must make a fundamental choice about the position of the front-end electronics. Obviously placing the electronics in an accessible region outside the detector vacuum chamber provides the most exibility as it allows manual adjustments, replacements, etc., without breaking the detector vacuum and removing the detector from the solenoid. Additionally, placing the electronics within the detector volume exposes these components to radiation damage and enhances the problem of heat dissipation from the electronics.

On the other hand, placing most of the electronics some distance away from the detector comes with significant disadvantages, as for example, the substantial cable volume and expense, the signal feedthroughs for the approximately 20,000 bipolar signals, and the increased noise and signal degradation. With respect to cable volume, if signals are transmitted from the preamps through the vacuum wall, then a set of ribbon coaxial cables about 5 cm thick surrounding the entire circumference of the detector are required.

Of course, all electronics must be positioned, in-so-far as possible beyond the turning radius of electrons of interest. This means that electronic boards must be placed radially around the detector at distances beyond the vanes. Mounting them on the detector supports requires active cooling and somewhat complicates the mechanical structure.

We choose here to discuss a tracker readout system designed to take advantage of modern electronic design using distributed signal processing [116]. All signals are digitized at the front end, and stored in digital pipelines for trigger latency. Once a trigger is presented, only those channels having signals above a set threshold are read, stored in buffers, and then serially transferred to a data acquisition system outside the vacuum wall. At this point the events are rebuilt, analyzed, filtered, and finally committed to permanent storage.

Suppose an electron track generates 60 electron-ion pairs. We propose to use a gas gain of 5×10^4 so the analog signal presented to the anode preamplifier will be 480 fC. We can assume that 10% of this charge is collected within the 6 ns which will be required for the signal to reach its peak. We should then set the discriminator threshold at approximately 16 fC or 2 primary electrons expecting a noise level of $\leq 1 - 2$ fC. The total capacitance of the straw is 30 pF and the characteristic impedance is 317Ω . Thus, we use a 200 series resistor coupled to a 100 transimpedance preamplifier. We expect the discriminator to have 2-3 ns timing resolution.

The ADC signal on the central strip should integrate to approximately 20% of the anode charge. This results in approximately 96 fC integrated over perhaps 70 ns. The ADC signal will be 20 – 100 fC, and to obtain the axial position resolution the ENC noise must be less than 1 – 2 fC. We then require 5 – 6 bit resolution in amplitude to discriminate against highly ionizing hits.

1.10.1 Noise

An induction strip surface area of $0.4 \text{ cm} \times 30 \text{ cm} = 12 \text{ cm}^2$ overlays 60 straws, and the strip capacitance is large, 30 – 75 pF. The count rate on the strips can be expressed as

$$N_{\text{pad}} = 5N_{\text{straw}} n \times w \times L ;$$

where N_{pad} and N_{straw} are the count rates of the pad strips and straw anodes, respectively, n is the number of straws covered by one pad, w is the width of the pad, and L is the length of the straw. Since one straw signal will induce charge on ~ 5 pads, the value of N_{pad} is about 200 kHz/pad or 40% of N_{straw} .

To reduce the noise and improve signal integrity, we propose to use a short segment of flexible cable, driven differentially by the strip and the signal ground plane. The cable is directly etched onto the strip without splicing. It should be no more than 30 cm long. The preamplifier (PP as discussed above) feeds a shielded digitizing circuit on the building block board. All signals are low-level, digital and analog grounds decoupled, and low voltage power isolated.

1.12 Signal Bus Lines

The total number of optical serial transfer lines will be ≤ 24 . Although this transfer is presently serial, it could be parallel transfer 16 bits wide. There are additional signals which must be sent to the tracker from the DAQ. These include;

- 1) a system clock which will be regenerated by the local bus sequencer;
- 2) a trigger input which could be associated with a readout quadrant of wires;
- 3) a sync(trigger reset) counter that determines the time stamp placed on the data ;
- 4) a system reset to return the readout to a standard operating condition;

- 5) a slow control bus that sends control signals and environmental monitor information;
- 6) low voltage power of +3.3V (300A) and -3.3V (100A)

1.10.2 Cable and Connections

Designs for vacuum feedthrough for multi-cable connections are available from other detectors. Even transmitting the signals from all channels through such a patch panel is possible, though not desirable. If we choose to use fiber optic links for data transfer, standard systems are installed at ATLAS, CMS, BABAR, and ALICE. We could choose to use an optic link to reduce system noise and it would require a very limited number of cables. Internal cables will be shielded and treated as transmission lines, and the design keeps all cables, including PCB lands as short as possible.

Transmission of the signals from the pads to the PP are identified as a major problem. Signals on these lines are small and must cross other lines and channels to reach the preamplifiers. The at panels on which the lines are etched must be thin, 25 μ m Kapton, which means shielding is not possible, and ground planes create large capacitance. Detailed research on this problem is needed.

1.10.3 Mounting and Servicing

Maintenance of the electronics must be reduced to minimum, as once installed in the vacuum it will not be easy to access the system. Therefore the design must be:

- robust and have adequate operational margins for thresholds, noise limits, and power;
- remotely controlled and have adequate diagnostic information supplied to an operator;
- redundant and sufficiently flexible that channels can be remotely removed without significantly impairing operations.

1.13 Transmitted Data Structure

The data structure is to be transmitted to the DAQ processor in the following sequence.

- 1) Begin Transfer header 1 16bit word
- 2) Buss number, Status
 - a) Header 2 16bit words
 - i) Trigger/time, ROC number, and status
 - b) Data 17 16bit words/channel
 - i) Channel number, length => 1 16bit word
 - ii) TDC => 1 16bit word
 - iii) Wave form => 15 16bit word

- c) Repeat Above for All ROC Controlled by a ROC
- 3) ROC number buss number 1 16bit word
- 4) Sequence through all ROCs
- 5) EOF

The local memory buffers are flushed into remote memory buffers placed in VME crates outside the detector solenoid. Each event is then reconstructed by assigning one processor in a farm to a particular trigger ID. This event is filtered by this processor for reconstructability and probability that it could be an event of interest. The filtered data set is then committed to permanent storage for off-line analysis. Sufficient data is stored, however, to allow a proper background analysis.

1.14 Low Voltage Power and Cooling

In a similar readout system (BaBar), the front end electronics expended 5 – 6 kW of low voltage power. It is possible that if the ICs are redesigned using more modern technology the power could be reduced. However 5 – 6 kw is not large and can be easily removed. We proposed to use chilled coolant, perhaps in association with the coolant used for the calorimeter, to maintain a reasonable and static temperature for the readout electronics.

Low voltage power will be separated into units supplying digital and front end analog ICs. Each board will use its own low-ripple regulator to provide its DC voltage. This arrangement reduces ground loop currents and isolates digital noise. Switching power supplies can be used for the digital ICs. The preamplifiers will use linear regulators to further reduce the power noise level down to less than 1 mVPP. We will evaluate the use of ferrite-core inductances in any power supplies in the cryostat.

We are considering optical links to transfer data to the Central Memory Farm to reduce noise, but rates are well within the capability of copper cable. If we do this we will require about 16 optical links from the 8 vane/plane units.

1.15 High Voltage

High voltage will be individually supplied to each vane and plane (16 separate units). The HV lines enter the downstream gas manifold and are then split to supply the 180 channels of straw anodes. Each channel must be fused in order to allow that channel to be removed in case of a malfunction. We envision this process occurring by passing a high current through the fused panel disabling a selected channel. Readout of a channel must occur through a HV blocking capacitor. All these components are within the gas volume contained within the manifold. The gas is held at atmospheric pressure so HV discharge should not present a problem.

We anticipate operational HV of the anode wires at about 2000 V to obtain a gas gain of 5×10^4 . The HV current variation between beam ash and data-active times may present a problem requiring lowering

the HV during periods of the beam-ash. This issue is still under evaluation. HV will be supplied by commercial units which are computer controlled and monitored.

1.16 Simulated response of the electronics

The results of a PSPICE simulation of a resistive straw detector have been compared to a series of measurements made with a prototype detector. These simulations well represent the measured parameters, and have then been used to undertale parametric studies on the effects of the detector and electronic parameters (e.g. cathode resistivity, and straw geometry). As an example, figure 3.2 shows the simulated response of the pads to an anode signal for various cathode resistivities. Table 4.1 are measured values.

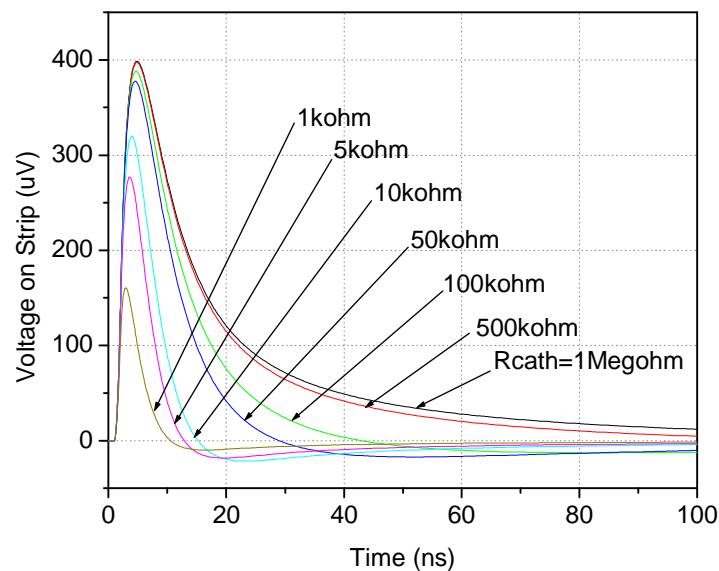


Figure 4.1: Screening effect of resistive cathode

Table 4.1: The Effect of Shielding on the Strip Signal Strength

Material	Copper Coated Mylar 25 μ m	Resistive Kapton 1k Ω /sq	Resistive Kapton 1Meg Ω /sq
Signal Change %	3.6	7-10	100
Simulation results	0	6	100

In order to study the anode signal delay, a 2.56m length a model was built using 640 circuit nodes. The straw is covered by strips over the full length. Figure 8.1 shows the anode signals when current source is positioned at the middle of a straw.

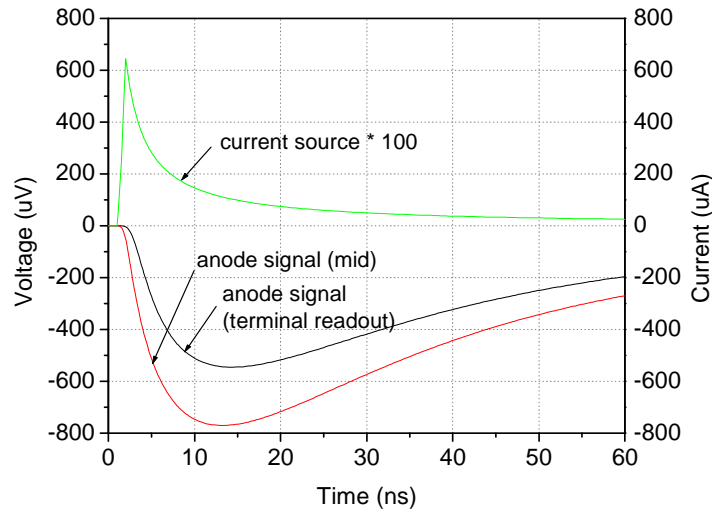


Figure 8.1: anode signal with current source in the middle of a straw

Compared to the current source, the anode signal has no significant time delay. The main current return path, in this case, is from the anode to strips to ground, and the signal flows along the transmission line between anode and cathode.

From all of these simulations, we draw the following conclusions.

- (1) The screening effect of the cathode is sensitive to its resistance. We need to keep the resistivity between $10\text{k}\Omega$ and $50\text{k}\Omega$, or we could use a larger resistivity if we use an external grounding trace to reduce the DC voltage drop on the cathode.
- (2) From the distribution of induced charge on the strips, we anticipate a position resolution for a point-charge on the anode of $<1/4$ of a strip width.
- (3) The resistive straw itself (without the strip for signal return) is a dispersive delay line, which delay and rise time of anode signal can be as large as several microseconds. Whenever a ground plane or strips was near the straws, the characteristic signal delay disappears.
- (4) The adjacent anode wires form the signal return path when there is no strip or ground plate. However, when strips or a ground plate exists, the low frequency current returns along the cathode to ground, and the high frequency current returns through the strips to ground.

1.18 References

```
\begin{references}
\bibitem{alt} R.Djilkibaev, MECO memo 051 (2000)
\bibitem{alt1} R.Djilkibaev and R.Konoplich, MECO memo 099 (2002)
\bibitem{alt2} R.Djilkibaev and R.Konoplich, MECO memo 113, hep-ex/0312022 (2003)
\bibitem{kalman} R.Fruhworth, NIM A262, 444-540 (1987)
\bibitem{daf} R.Fruhworth and A.Stradlie Comp. Phys. Communication 120, 197-214 (1999)
\bibitem{GSF} R.Fruhworth, Comp. Phys. Communication 100, 1-16 (1997)
\bibitem{Kit} G.Kitagawa, Ann. Inst. Statist. Math. 46, 605 (1994)
\end{references}
```


\begin{references}
\bibitem{alt} R.Djilkibaev, MECO memo 051 (2000)
\bibitem{alt1} R.Djilkibaev and R.Konoplich, MECO memo 099 (2002)
\bibitem{alt2} R.Djilkibaev and R.Konoplich, MECO memo 113, hep-ex/0312022 (2003)
\bibitem{alt3} R.Djilkibaev and R.Konoplich, MECO memo 123 (2004)
\bibitem{kalman} R.Fruhworth, NIM A262, 444-540 (1987)
\bibitem{daf} R.Fruhworth and A.Stradlie Comp. Phys. Communication 120, 197-214 (1999)
\bibitem{GSF} R.Fruhworth, Comp. Phys. Communication 100, 1-16 (1997)
\bibitem{Kit} G.Kitagawa, Ann. Inst. Statist. Math. 46, 605 (1994)
\bibitem{benussi} L. Benussi, {\it et al}, {\bf NIM A419}(1998)648.
\bibitem{bondarenko} V. Bondarenko,
{\it et al}, Atlas Memo {INDET-NO-010}(1992).
\bibitem{straws} V. Bondarenko, {\it et al}, Atlas Memo {INDET-NO-010}(1992);
S. H. Oh, {\it et al}, {\bf NIM A309}(1991)368;
R. Cizeron, {\it et al}, {\bf NIM A307}(1991)286;
G. Bonvichi, {\it et al}, {\bf NIM A359}(1995)492;
C. Brand, {\it et al}, {\bf NIM A367}(1995)129;
\bibitem{induction} S. Majewski, {\it et al}, {\bf NIM A348}(1994)307;
N. Khovansky {\it et al}, {\bf NIM A351}(1994)317;
V. N. Bychkov, {\it et al}, {\bf NIM A325}(1993)158;
C. Leonidopoulos, {\it et al}, {\bf NIM A427}(1999)465;
J. Marzec, {\it et al}, {\bf IEEE Trans. Nucl. Sci. 47}(2000)18;
P. Fisher, {\it et al}, {\bf IEEE
Trans. Nucl. Sci. 35}(1998)432
\bibitem{mathieson} J. Gordan and E. Mathieson,
{\bf NIM A227}(1984)267; {\bf A235}(1985)505; {\bf A270}(1988)602.
\bibitem{electronics} F. M. Newcomer, {\it et al},
{\bf IEEE Trans. Nucl. Sci. 43}(1996)1725;
T. Akesson, {\it et al}, {\bf NIM 449}(2000)446;
R. L. Chase, {\it et al}, {\bf NIM A409}(1998)328
\bibitem{babar} S. F. Dow, {\it et al}, {\bf IEEE
Trans. Nucl. Sci. 46}(1999)785;
A. J. Lanford, {\bf NIM409},(1998)654.
J. Albert, {\it et al}, {\bf IEEE Trans. Nucl. Sci. }(1999)
\bibitem{vacuum} G. De Cataldo, {\it et al}, {\bf NIM A409}(1998)73;
E. Barbarito, {\it et al}, {\bf NIM A381}(1996)39.
\bibitem{gas} J. M. Butler, {\it et al}, {\bf NIM A290}(1990)122;
J. Fischer, {\it et al}, {\bf NIM A238}(1985)249;
R. Openshaw, {\it et al}, {\bf IEEE Trans. Nucl. Sci. 36}(1989)567;
J. Wise, J. A. Kadyk, and D. Wiltess, J. App. Phys. {\bf 74}(1993)5327;
\bibitem{unknown} ?, {\bf NIM A381}(1996)372.
[1] C. Leonidopoulos, et al., “Development of a straw tube chamber with pick up-pad readout”,
Nuclear Instruments and Methods in Physics Research A427(1999)465-486.
[2] Veljko Radeka, Instrumentation Division, Brookhaven National Laboratory, private
communication.
[3] S. Tsui, et al., “A Short Resistive Straw Prototype”, MECO-UH-01, “First Resistive Straw
Prototype Report” University of Houston, Internal Report, 2001.
[4] Kapton XC100, a polyimide film manufactured by Dupont, Inc.

- [5] Janusz Marzec, et al., "Signal Propagation in Straw Tubes with Resistive Cathode", IEEE Transactions on Nuclear Science, 47(2000)18-24.
- [6] reference software.
- [7] K. Lau, et al., "Test Results of a High Precision Cathode Strip Chamber Based on Plastic Streamer Tubes", Nuclear Instruments and Methods in Physics Research A354(1995)376-388.
- [8] Kwong Lau, et al., "Optimization of Centroid-finding Algorithms for Cathode Strip Chambers", Nuclear Instruments and Methods in Physics Research A366(1995)298-309.
- [9] J. S. Gordon, E. Mathieson, "Cathode Charge Distribution in Multiwire Chambers I. Measurement and Theory", Nuclear Instruments and Methods in Physics Research A227(1984)267-276.
- [10] E. Mathieson, J. S. Gordon, "Cathode Charge Distribution in Multiwire Chambers II. Approximate and empirical Formulae", Nuclear Instruments and Methods in Physics Research A227(1984)277-282.
- [11] V. Radeka, "Low-noise Techniques in Detectors", Nucl. Part. Sci. 38(1988)217-277
- [12] Konrad Kleinknecht, "Detectors for Particle Radiation", 2nd edition, Cambridge University Press, 1998

\bibitem{drift_papers}W. Bloom and L. Rolandi, {\bf Particle Detection with Drift Chambers}, Springer-Verlag, 1993

\bibitem{cern}http://ref.cern.ch/CERN/CNL/2000/001/garfield

\bibitem{mega}M. Barakat, {\it et al}, Nucl. Inst. and Meth. {\bf A349}(1994)118; M. Ahmed, {\it et al}, Phys. Rev. {\bf D65}(2002)112002

\bibitem{vavilov}P. V. Vavilov, Sov. Phys. JEPT {\bf 5}(1957)749;

L. D. Landau, J. Phys USSR {\bf 8}(1944)201

\bibitem{eloss}{\bf Review of particle Properties}, Phys. Rev. {\bf D66}(2002)010001-195; U. Fano, Ann. Rev. Nucl. Sci. {\bf 13}(1963)1

\bibitem{dc_book}I. Lehrs, {\it et al}, Nucl. Inst. and Meth. {\bf 153}(1982)361.

\bibitem{sauli}G. Charpak and F. Sauli, Ann. Rev. Nucl. Sci. {\bf 34}(1984)189; F. Sauli, CERN Report77-09, 1977

\bibitem{barcus}S. M. Seltzer and M. J. Berger, Int. J. Rad. Isotope {\bf 33}(1982)1189

\bibitem{gas_book}L. Loeb, {\bf Basic Processes of Gaseous Electronics}, Univ. Calif. Press., (1960)

begin{thebibliography}{10}

\bibitem{rsvp}MECO collaboration, {\bf Rare Symmetry Violating Processes}, proposal, 1999

\bibitem{discussion_1}D. Zimmerman, Private discussion

\bibitem{plate_theory}S. Timoshenko, {\bf Theory of Plates and Shells}, McGraw-Hill, 1940

\bibitem{discussion_2}E. Hungerford, Private discussion

\ references

[1]

[2] "A bipolar front-end integrated circuit for the BaBar helium drift chamber", D. Dorfan et al., Nucl. Instr. Meth. A409 (1998) 310.

[3] "The ALTRO Chip: A 16-Channel A/D Converter and Digital Processor for Gas Detectors", R. Esteve Bosch et al., IEEE Trans. Nucl. Sci.

